

# Climate change analysis from LRD manifold functional regression

Diana P. Ovalle–Muñoz<sup>1</sup>, M. Dolores Ruiz–Medina<sup>1</sup>

<sup>1</sup> Department of Statistics and Operation Research, University of Granada

## Abstract

A functional nonlinear regression approach, incorporating time information in the covariates, is proposed for temporal strong correlated manifold map data sequence analysis. Specifically, the functional regression parameters are supported on a connected and compact two–point homogeneous space. The Generalized Least–Squares (GLS) parameter estimator is computed in the linearized model, having error term displaying manifold scale varying Long Range Dependence (LRD). The performance of the theoretical and plug–in nonlinear regression predictors is illustrated by simulations on sphere, in terms of the empirical mean of the computed spherical functional absolute errors. In the case where the second–order structure of the functional error term in the linearized model is unknown, its estimation is performed by minimum contrast in the functional spectral domain. The linear case is illustrated in the Supplementary Material, revealing the effect of the slow decay velocity in time of the trace norms of the covariance operator family of the regression LRD error term. The purely spatial statistical analysis of atmospheric pressure at high cloud bottom, and downward solar radiation flux in [1] is extended to the spatiotemporal context, illustrating the numerical results from a generated synthetic data set.

*Keywords* Connected and compact two–point homogeneous spaces, LRD manifold functional time series, temporal strong correlated manifold map data, manifold multiple functional regression.

## 1 Introduction

The strong effect of climate changes in solar radiation in several ways through atmospheric components has been extensively studied. That is the case of the increase in greenhouse gases can trap more heat in the atmosphere, leading to an increase in Earth’s surface temperature. Additionally, the presence of atmospheric aerosols, such as smog or pollution particles, can scatter solar radiation,

which can have local effects on the amount of energy reaching the Earth's surface. In particular, the interaction between distribution and intensity of solar radiation, and atmospheric pressure patterns seriously affects regional and global climate systems (see, e.g., [13]; [26]). Particularly, a purely spatial statistical analysis of atmospheric pressure at high cloud bottom, and downward solar radiation flux has been achieved in [1] in the framework of spherical isotropic random fields, from a nonparametric bayesian perspective. This research area motivates the manifold infinite-dimensional nonlinear regression approach presented with temporal long-memory isotropic manifold functional error term. In particular, the downward solar radiation flux earth map prediction problem, from observed atmospheric pressure at high cloud bottom is addressed here. This issue has strong impact in climate change analysis. That is the case of solar radiation on surface inducing high temperatures and evaporation, or the relationship between atmospheric pressure, and precipitation, among others, affecting the Hydrological Cycle.

The proposed functional predictive framework also supposes a substantial contribution in the field of spatiotemporal regression from a functional perspective, leading to the analysis of the evolution of manifold map data sequences correlated in time. The temporal correlation is represented in a flexible way interacting with the spatial scale, i.e., allowing different long range dependence levels depending on the spatial scales. The statistical methodology proposed is quite flexible although it requires the application of sophisticated mathematical tools (e.g., infinite-dimensional spectral analysis). However, as illustrated in the present paper, the computational cost and complexity of its implementation can be substantially reduced under the scenario analyzed of invariance of the involved covariance kernels, with respect to the group of isometries of the manifold  $\mathbb{M}_d$ , with  $d$  being its topological dimension. Such kernels admit a diagonal representation in terms of the eigenfunctions of the Laplace-Beltrami operator.

We adopt the separable Hilbert space framework of  $H = L^2(\mathbb{M}_d, d\nu)$  of  $\mathbb{M}_d$ -supported functional data under square-integrability with respect to the normalized Riemannian measure  $d\nu$  on  $\mathbb{M}_d$ . Our functional regression modeling framework goes beyond the structural assumptions present, for instance, in [3]; [11]; [12]; [5]; [8]; [10]; [17]; [20]; [21]; [22], and references therein. It also supposes an extension to the nonlinear, non Euclidean, and Long-Range Dependence (LRD) settings of the FANOVA analysis under dependent errors achieved in [23], as well as of the subsequent contributions addressed in [25] for multiple regression, and in [2] for fixed effect models including the case of circular domains. The second order properties of the error term in the linearized model, including spatial-scale-varying LRD, are characterized via a semiparametric framework in the spectral domain, following the multifractional integration approach for functional time series in [18], and [24]. Indeed, in this framework, an extended approach respect to the one given in [15] is adopted, since in that paper only the context of fractional integration of functional time series can be addressed. Note that, in our manifold scale varying spectral anal-

ysis, Short Range Dependence (SRD) condition assumed in [19] is not required (see also [7], and [6] where SRD spherical functional time series are introduced and analyzed).

As pointed out in [1], the averaging over time achieved in its purely spatial analysis of bivariate atmospheric pressure and downward solar radiation flux data, can cause information lost about possibly important temporal patterns in these data. To overcome this drawback our manifold functional regression model incorporates time evolution. We adopt the generalized least squares estimation strategy in the approximation of the manifold-supported functional regression parameters defining the functional regression predictor in the linearized model. Under a misspecified scenario, our plug-in nonlinear regression predictor is constructed from the estimation of the spectral density operator family characterizing the second-order structure of the functional error term in the linearized model. Specifically, a minimum contrast estimation strategy is considered in the approximation of the parametric pure point spectrum of the long-range dependence operator at the direct sum of the eigenspaces of the Laplace Beltrami operator where the projected linearized process displays LRD. The asymptotic analysis of the regression predictor can be conducted in a similar way to [25] in the linearized model.

The outline of the paper is as follows. Section 2 presents some preliminary elements on the spectral analysis of LRD manifold functional time series. Section 3 introduces our multiple functional regression setting in a parametric nonlinear framework. The generalized least-squares estimator of the manifold functional regression parameter vector is then computed in the linearized model, as well as the linear and nonlinear regression predictors. In Section 4, a simulation study is undertaken to illustrate the performance of the theoretical and plug-in nonlinear regression predictors, under an infinite-dimensional log-Gaussian scenario. See also Section 1 in the Supplementary Material where the prediction methodology proposed is illustrated in the context of spherical functional fixed effect models. Indeed, for this family of spherical functional linear models, the asymptotic and finite functional sample properties of the theoretical and plug-in regression predictors are illustrated. Particularly, the effect of the pure point spectral patterns of the LRD operator of the regression error, affecting accuracy and variability of GLS plug-in parameter estimator, is analyzed. The main practical motivation of this paper arises in Section 5, where downward solar radiation flux earth maps functional prediction is achieved from atmospheric pressure at high cloud bottom, considering a generated synthetic data set. Some final comments and open research lines are discussed in Section 6.

## 2 Preliminaries

Let  $X = \{X(\mathbf{x}, t), \mathbf{x} \in \mathbb{M}_d, t \in \mathbb{T}\}$  be a zero-mean, stationary in time, and isotropic in space mean-square continuous Gaussian, or elliptically contoured,

spatiotemporal random field on the basic probability space  $(\Omega, \mathcal{A}, P)$ , with covariance function  $C(d_{\mathbb{M}_d}(\mathbf{x}, \mathbf{y}), t-s) = E[X(\mathbf{x}, t)X(\mathbf{y}, s)]$ , for  $\mathbf{x}, \mathbf{y} \in \mathbb{M}_d$ , and  $t, s \in \mathbb{T}$ . Here,  $\mathbb{T}$  denotes the temporal domain, which can be  $\mathbb{Z}$  or  $\mathbb{R}$ . Under the conditions of Theorem 4 in [16], the covariance function  $C(d_{\mathbb{M}_d}(\mathbf{x}, \mathbf{y}), t-s)$  admits the following diagonal series expansion:

$$\begin{aligned} C(d_{\mathbb{M}_d}(\mathbf{x}, \mathbf{y}), t-s) &= \sum_{n \in \mathbb{N}_0} B_n(t-s) \sum_{j=1}^{\delta(n,d)} S_{n,j}^d(\mathbf{x}) S_{n,j}^d(\mathbf{y}) \\ &= \sum_{n \in \mathbb{N}_0} \frac{\delta(n,d)}{\omega_d} B_n(t-s) R_n^{(\alpha,\beta)}(\cos(d_{\mathbb{M}_d}(\mathbf{x}, \mathbf{y}))), \quad \mathbf{x}, \mathbf{y} \in \mathbb{M}_d, \quad t, s \in \mathbb{T}, \end{aligned} \quad (1)$$

where  $\delta(n, d)$  denotes the dimension of the  $n$ th eigenspace  $H_n$  of the Laplace Beltrami operator,  $\omega_d = \int_{\mathbb{M}_d} d\nu(\mathbf{x})$ , and  $\{S_{n,j}^d, j = 1, \dots, \delta(n, d), n \in \mathbb{N}_0\}$  is the system of orthonormal eigenfunctions of the Laplace Beltrami operator  $\Delta_d$  on  $L^2(\mathbb{M}_d, d\nu, \mathbb{R})$ . Furthermore, in the last identity in (1), we have applied addition formula in the context of connected and compact two-point homogeneous spaces (see Theorem 3.2 in [14] and p. 455 in [4]), where  $R_n^{\alpha,\beta}(\cos(d_{\mathbb{M}_d}(\mathbf{x}, \mathbf{y}))) = \frac{P_n^{\alpha,\beta}(\cos(d_{\mathbb{M}_d}(\mathbf{x}, \mathbf{y})))}{P_n^{\alpha,\beta}(1)}$ , with  $P_n^{\alpha,\beta}$  denoting the Jacobi polynomial of degree  $n \in \mathbb{N}_0$ , with parameters  $\alpha$  and  $\beta$  (see, e.g., [16], and [9], for more details on Lie Algebra based approach).

Consider the restriction  $X_T = \{X(\mathbf{x}, t), \mathbf{x} \in \mathbb{M}_d, t \in [0, T]\}$  of  $X$  satisfying (1) to the interval  $[0, T]$ . The following lemma provides the orthogonal expansion of  $X_T = \{X(\mathbf{x}, t), \mathbf{x} \in \mathbb{M}_d, t \in [0, T]\}$  in terms of the eigenfunctions of the Laplace Beltrami operator (see Theorem 1 in the Supplementary Material in [18]).

**Lemma 1** *Let  $X_T = \{X(\mathbf{x}, t), \mathbf{x} \in \mathbb{M}_d, t \in [0, T]\}$  be the restriction of  $X$  to the interval  $[0, T]$ , satisfying (1), and*

$$\sum_{n \in \mathbb{N}_0} B_n(0) \delta(n, d) < \infty. \quad (2)$$

*Then,  $X_T$  admits the following orthogonal expansion:*

$$X_T(\mathbf{x}, t) \stackrel{\mathcal{L}_{\tilde{H}}^2(\Omega, \mathcal{A}, P)}{=} \sum_{n \in \mathbb{N}_0} \sum_{j=1}^{\delta(n,d)} V_{n,j}(t) S_{n,j}^d(\mathbf{x}), \quad \mathbf{x} \in \mathbb{M}_d, \quad t \in [0, T], \quad (3)$$

where  $\mathcal{L}_{\tilde{H}}^2(\Omega, \mathcal{A}, P) = L^2(\Omega \times \mathbb{M}_d \times [0, T], P(d\omega) \otimes d\nu \otimes dt)$ , with  $\tilde{H} = L^2(\mathbb{M}_d \times [0, T], d\nu \otimes dt)$ . Here,  $\{V_{n,j}(t), t \in [0, T], j = 1, \dots, \delta(n, d), n \in \mathbb{N}_0\}$  is a sequence of centered uncorrelated random processes on  $[0, T]$  given by

$$V_{n,j}(t) = \int_{\mathbb{M}_d} X_T(\mathbf{y}, t) S_{n,j}^d(\mathbf{y}) d\nu(\mathbf{y}), \quad j = 1, \dots, \delta(n, d), \quad n \in \mathbb{N}_0, \quad (4)$$

in the mean-square sense.

Assume that  $\mathbb{T} = \mathbb{Z}$ , and that the map

$$\tilde{X}_t : (\Omega, \mathcal{A}) \longrightarrow (L^2(\mathbb{M}_d, d\nu, \mathbb{R}), \mathcal{B}(L^2(\mathbb{M}_d, d\nu, \mathbb{R})))$$

is measurable, with  $\tilde{X}_t(\mathbf{x}) := X(\mathbf{x}, t)$  for every  $t \in \mathbb{T}$  and  $\mathbf{x} \in \mathbb{M}_d$ . Here,  $\mathcal{B}(L^2(\mathbb{M}_d, d\nu, \mathbb{R}))$  denotes the Borel  $\sigma$ -algebra on  $L^2(\mathbb{M}_d, d\nu, \mathbb{R})$  (i.e., the smallest  $\sigma$ -algebra containing the collection of all open subsets of  $L^2(\mathbb{M}_d, d\nu, \mathbb{R})$ ). By previous assumptions on  $X$ ,  $\{\tilde{X}_t, t \in \mathbb{Z}\}$  then defines a manifold weak-sense stationary functional time series. In particular,  $E[\tilde{X}_t] = 0$ , and  $\sigma_{\tilde{X}}^2 = E[\|\tilde{X}_t\|_{L^2(\mathbb{M}_d, d\nu, \mathbb{R})}^2] = E[\|\tilde{X}_0\|_{L^2(\mathbb{M}_d, d\nu, \mathbb{R})}^2] = \|R_0\|_{L^1(L^2(\mathbb{M}_d, d\nu, \mathbb{R}))}$ , for every  $t \in \mathbb{Z}$ . By  $L^1(L^2(\mathbb{M}_d, d\nu, \mathbb{R}))$  we denote the space of trace or nuclear operators on  $L^2(\mathbb{M}_d, d\nu, \mathbb{R})$ . The second-order structure of  $\{\tilde{X}_t, t \in \mathbb{Z}\}$  is characterized by the family of covariance operators  $\{\mathcal{R}_t, t \in \mathbb{Z}\}$  given by, for all  $h, g \in L^2(\mathbb{M}_d, d\nu, \mathbb{R})$ ,

$$\begin{aligned} \mathcal{R}_t(g)(h) &= E[\tilde{X}_{s+t}(h)\tilde{X}_s(g)] = E\left[\left\langle \tilde{X}_{s+t}, h \right\rangle_{L^2(\mathbb{M}_d, d\nu, \mathbb{R})} \left\langle \tilde{X}_s, g \right\rangle_{L^2(\mathbb{M}_d, d\nu, \mathbb{R})}\right] \\ \mathcal{R}_t &:= E[\tilde{X}_{s+t} \otimes \tilde{X}_s] = \quad \forall t, s \in \mathbb{Z}. \end{aligned} \quad (5)$$

Let  $\{\tilde{X}_t, t \in \mathbb{Z}\}$  be, as before, a weak-sense stationary centered functional time series with values in the space  $L^2(\mathbb{M}_d, d\nu, \mathbb{R})$ . Under (1), the family of its covariance operators  $\{\mathcal{R}_t, t \in \mathbb{Z}\}$  satisfies

$$\mathcal{R}_t = E[\tilde{X}_t \otimes \tilde{X}_0] = \sum_{n \in \mathbb{N}_0} B_n(t) \sum_{j=1}^{\delta(n,d)} S_{n,j}^d \otimes S_{n,j}^d, \quad t \in \mathbb{Z}. \quad (6)$$

Now, the main elements involved in the spectral analysis of functional time series are briefly introduced in our LRD setting. Specifically, the spectral density operator family  $\{\mathcal{F}_\omega, \omega \in [-\pi, \pi]\}$  is given by

$$\mathcal{F}_\omega \underset{\mathcal{S}(L^2(\mathbb{M}_d, d\nu, \mathbb{C}))}{=} \frac{1}{2\pi} \sum_{t \in \mathbb{Z}} \exp(-i\omega t) \mathcal{R}_t, \quad \omega \in [-\pi, \pi] \setminus \{0\}, \quad (7)$$

where  $\underset{\mathcal{S}(L^2(\mathbb{M}_d, d\nu, \mathbb{C}))}{=}$  denotes the identity in the norm of the space of Hilbert-Schmidt operators. From equations (6) and (7),

$$\begin{aligned} \mathcal{F}_\omega \underset{\mathcal{S}(L^2(\mathbb{M}_d, d\nu, \mathbb{C}))}{=} & \sum_{n \in \mathbb{N}_0} \left[ \sum_{t \in \mathbb{Z}} \exp(-i\omega t) B_n(t) \right] \sum_{j=1}^{\delta(n,d)} S_{n,j}^d \otimes S_{n,j}^d \\ \underset{\mathcal{S}(L^2(\mathbb{M}_d, d\nu, \mathbb{C}))}{=} & \sum_{n \in \mathbb{N}_0} f_n(\omega) \sum_{j=1}^{\delta(n,d)} S_{n,j}^d \otimes S_{n,j}^d, \end{aligned}$$

with

$$B_n(t) = \int_{[-\pi, \pi]} \exp(i\omega t) f_n(\omega) d\omega, \quad \forall t \in \mathbb{Z}. \quad (8)$$

The functional Discrete Fourier Transform fDFT  $\tilde{X}_\omega^{(T)}(\cdot)$  of the manifold map data is defined as

$$\tilde{X}_\omega^{(T)}(\cdot) \stackrel{L^2(\mathbb{M}_d, d\nu, \mathbb{C})}{=} \frac{1}{\sqrt{2\pi T}} \sum_{t=1}^T \tilde{X}_t(\cdot) \exp(-i\omega t), \quad \omega \in [-\pi, \pi], \quad (9)$$

where  $\stackrel{L^2(\mathbb{M}_d, d\nu, \mathbb{C})}{=}$  denotes the equality in  $L^2(\mathbb{M}_d, d\nu, \mathbb{C})$  norm, with  $L^2(\mathbb{M}_d, d\nu, \mathbb{C})$  being the complex version of the Hilbert space  $L^2(\mathbb{M}_d, d\nu, \mathbb{R})$ . Note that  $\tilde{X}_\omega^{(T)}(\cdot)$  is a random element in the space  $L^2(\mathbb{M}_d, d\nu, \mathbb{C})$ , since

$$E \left[ \|\tilde{X}_\omega^{(T)}\|_{L^2(\mathbb{M}_d, d\nu, \mathbb{C})} \right] \leq \frac{1}{\sqrt{2\pi T}} \sum_{t=1}^T E \|\tilde{X}_t(\cdot)\|_{L^2(\mathbb{M}_d, d\nu, \mathbb{R})} < \infty.$$

As usually, the periodogram operator is defined from the fDFT by  $p_\omega^{(T)} = \tilde{X}_\omega^{(T)} \otimes \overline{\tilde{X}_\omega^{(T)}} = \tilde{X}_\omega^{(T)} \otimes \tilde{X}_{-\omega}^{(T)}$ . Its mean is then computed as

$$\begin{aligned} E[p_\omega^{(T)}] &= E[\tilde{X}_\omega^{(T)} \otimes \tilde{X}_{-\omega}^{(T)}] = \frac{1}{2\pi} \sum_{u=-(T-1)}^{T-1} \exp(-i\omega u) \frac{(T-|u|)}{T} \mathcal{R}_u \\ &= \int_{-\pi}^{\pi} F_T(\omega - \xi) \mathcal{F}_\xi d\xi, \quad T \geq 2, \end{aligned}$$

in terms of the Féjer kernel  $F_T(\omega) = \frac{1}{T} \sum_{t=1}^T \sum_{s=1}^T \exp(-i(t-s)\omega)$ .

### 3 Multiple functional regression in manifolds

As given in Section 5 on the real-data application, the evolution of geophysical phenomena are usually governed by nonlinear equations. In particular, in this section these equations define the trend of our response in a nonlinear way from the observed covariates. These covariates are introduced as the observation of random magnitudes, possibly governed by nonlinear equations depending on time and space, involving a random initial condition. That is the case of the barometric equation defining atmospheric pressure at high cloud bottom in Section 5, where we have considered the initial pressure at medium-low altitudes as the random initial condition, since, in our observation model, random fluctuations are induced by unknown heights, where atmospheric pressure measurements are taken in the height range given by the interval (6000, 12000) meters. Note that in the real-data example in Section 5, we analyze the evolution of nonlinear functional association between the atmospheric pressure at high cloud

bottom, and the downward solar radiation flux. The last one displays changes in its spherical patterns with the latitude, affected by the observed atmospheric pressure during the studied period autumn–winter. In that period, medium and high latitude areas (in both hemispheres) display low atmospheric pressure, while subtropical and tropical regions display high atmospheric pressure. Note that the reverse situation occurs in spring–summer.

The following manifold multiple functional nonlinear regression model is introduced:

$$\mathbf{Y}(\mathbf{x}) = \mathbf{H}(\mathbf{X}(\boldsymbol{\beta}))(\mathbf{x}) + \boldsymbol{\varepsilon}(\mathbf{x}) \quad \mathbf{x} \in \mathbb{M}_d, \quad (10)$$

where

$$\begin{aligned} \mathbf{X} &= (X_{t,j})_{t=1,\dots,T;j=1,\dots,p}; \quad \mathbf{Y}(\mathbf{x}) = [Y_1(\mathbf{x}), Y_2(\mathbf{x}), \dots, Y_T(\mathbf{x})]^T, \\ \boldsymbol{\beta}(\mathbf{x}) &= [\beta_1(\mathbf{x}), \dots, \beta_p(\mathbf{x})]^T; \quad \boldsymbol{\varepsilon}(\mathbf{x}) = [\varepsilon_1(\mathbf{x}), \varepsilon_2(\mathbf{x}), \dots, \varepsilon_T(\mathbf{x})]^T, \end{aligned}$$

for every  $\mathbf{x} \in \mathbb{M}_d$ . Here,  $\beta_j \in L^2(\mathbb{M}_d, d\nu, \mathbb{R})$  provides the spatial weighting of temporal covariates  $X_{t,j} \in \mathbb{R}$ ,  $t = 1, \dots, T$ ,  $j = 1, \dots, p$  (e.g., time–varying Fourier coefficients of a spatiotemporal magnitude with respect to a purely spatial basis). The isomorphic operator  $\mathbf{H} : [L^2(\mathbb{M}_d, d\nu, \mathbb{R})]^T \rightarrow [L^2(\mathbb{M}_d, d\nu, \mathbb{R})]^T$  combines geographical and temporal information affecting the functional response  $\mathbf{Y}$  in a nonlinear manner. Here,  $[L^2(\mathbb{M}_d, d\nu, \mathbb{R})]^T$  denotes the space of  $T$ –dimensional vector functions with the inner product

$$\langle \mathbf{f}, \mathbf{g} \rangle_{[L^2(\mathbb{M}_d, d\nu, \mathbb{R})]^T} = \sum_{l=1}^T \langle f_l, g_l \rangle_{L^2(\mathbb{M}_d, d\nu, \mathbb{R})},$$

for every  $\mathbf{f} = (f_1, \dots, f_T)^T$ ,  $\mathbf{g} = (g_1, \dots, g_T)^T \in [L^2(\mathbb{M}_d, d\nu, \mathbb{R})]^T$ .

Along the paper we assume that the error term  $\{\varepsilon_t, t \in \mathbb{Z}\}$  is such that  $\{\tilde{\varepsilon}_t = \mathbf{H}^{-1}(\varepsilon_t), t \in \mathbb{Z}\}$  is an LRD stationary centered functional time series, with values in the space  $L^2(\mathbb{M}_d, d\nu, \mathbb{R})$ , having invariant covariance operator family, satisfying the conditions assumed in Theorem 4 in [16] and in Lemma 1. Hence,  $\tilde{\boldsymbol{\varepsilon}}(\mathbf{x}) = [\mathbf{H}^{-1}(\varepsilon_1)(\mathbf{x}), \mathbf{H}^{-1}(\varepsilon_2)(\mathbf{x}), \dots, \mathbf{H}^{-1}(\varepsilon_T)(\mathbf{x})]^T$  has matrix covariance operator

$$\begin{aligned} \mathbf{R}_{\tilde{\boldsymbol{\varepsilon}}\tilde{\boldsymbol{\varepsilon}}} &= E \left[ \tilde{\boldsymbol{\varepsilon}}(\cdot) \tilde{\boldsymbol{\varepsilon}}^T(\cdot) \right] \\ &= \begin{bmatrix} E \left[ \mathbf{H}^{-1}(\varepsilon_1)(\cdot) \otimes \mathbf{H}^{-1}(\varepsilon_1)(\cdot) \right] & \cdots & E \left[ \mathbf{H}^{-1}(\varepsilon_1)(\cdot) \otimes \mathbf{H}^{-1}(\varepsilon_T)(\cdot) \right] \\ E \left[ \mathbf{H}^{-1}(\varepsilon_2)(\cdot) \otimes \mathbf{H}^{-1}(\varepsilon_1)(\cdot) \right] & \cdots & E \left[ \mathbf{H}^{-1}(\varepsilon_2)(\cdot) \otimes \mathbf{H}^{-1}(\varepsilon_T)(\cdot) \right] \\ \vdots & \vdots & \vdots \\ E \left[ \mathbf{H}^{-1}(\varepsilon_T)(\cdot) \otimes \mathbf{H}^{-1}(\varepsilon_1)(\cdot) \right] & \cdots & E \left[ \mathbf{H}^{-1}(\varepsilon_T)(\cdot) \otimes \mathbf{H}^{-1}(\varepsilon_T)(\cdot) \right] \end{bmatrix} \\ &= \begin{bmatrix} R_0 & R_1 & \cdots & R_{T-1} \\ R_1 & R_0 & \cdots & R_{T-2} \\ \vdots & \vdots & \vdots & \\ R_{T-1} & R_{T-2} & \cdots & R_0 \end{bmatrix}. \end{aligned}$$

The functional entries of  $\mathbf{R}_{\tilde{\varepsilon}\tilde{\varepsilon}}$  then admit the diagonal series expansion given in equation (1). In the subsequent development we will consider the orthogonal expansion of  $\mathbb{M}_d$ -supported functions  $\beta_h$ ,  $h = 1, 2, \dots, p$ , given by

$$\beta_h(\mathbf{x}) = \sum_{n \in \mathbb{N}_0} \sum_{k=1}^{\delta(n,d)} \beta_{n,k}^{(h)} S_{n,k}^d(\mathbf{x}), \quad \forall \mathbf{x} \in \mathbb{M}_d, \quad (11)$$

where  $\beta_{n,k}^{(h)} = \left\langle \beta_h, S_{n,k}^d \right\rangle_{L^2(\mathbb{M}_d, d\nu, \mathbb{R})}$ , for every  $k = 1, \dots, \delta(n,d)$ ,  $n \in \mathbb{N}_0$ , and  $h = 1, 2, \dots, p$ .

From the conditions assumed on the error term, the restriction of  $\{\mathbf{H}^{-1}(Y_t), t \in \mathbb{Z}\}$  to the interval  $[0, T]$  also admits the orthogonal expansion in the space  $\mathcal{L}_{\tilde{H}}^2(\Omega, \mathcal{A}, P) = L^2(\Omega \times \mathbb{M}_d \times [0, T], P(d\omega) \otimes d\nu \otimes dt)$

$$\tilde{Y}_t = \mathbf{H}^{-1}(Y_t)(\mathbf{x}) = \sum_{n \in \mathbb{N}_0} \sum_{j=1}^{\delta(n,d)} \tilde{Y}_{n,j}(t) S_{n,j}^d(\mathbf{x}), \quad \forall \mathbf{x} \in \mathbb{M}_d, \quad (12)$$

where  $\tilde{\mathbf{Y}}_{n,j} = \left( \left\langle \tilde{Y}_1, S_{n,j}^d \right\rangle_{L^2(\mathbb{M}_d, d\nu, \mathbb{R})}, \dots, \left\langle \tilde{Y}_T, S_{n,j}^d \right\rangle_{L^2(\mathbb{M}_d, d\nu, \mathbb{R})} \right)^T$ , for  $j = 1, \dots, \delta(n,d)$ , and  $n \in \mathbb{N}_0$ .

### 3.1 GLS functional parameter estimation

According to equation (8), applied to the case  $\tilde{X}_t = \tilde{\varepsilon}_t$ , for every  $t \in \mathbb{Z}$ , one can consider the matrix sequence

$$\left\{ \mathbf{\Lambda}_n = \begin{bmatrix} B_n(0) & \cdots & B_n(T-1) \\ \vdots & \ddots & \vdots \\ B_n(T-1) & \cdots & B_n(0) \end{bmatrix}, \quad n \in \mathbb{N}_0 \right\} \\ = \left\{ \int_{[-\pi, \pi]} \begin{bmatrix} f_n(\omega) & \cdots & \exp(i\omega(T-1)) f_n(\omega) \\ \vdots & \ddots & \vdots \\ \exp(i\omega(T-1)) f_n(\omega) & \cdots & f_n(\omega) \end{bmatrix} d\omega, \quad n \in \mathbb{N}_0 \right\} \quad (13)$$

where here we have denoted by  $B_n(t)$ ,  $t = 0, \dots, T-1$ , the time-varying coefficients in the series expansion of the functional entries of  $\mathbf{R}_{\tilde{\varepsilon}\tilde{\varepsilon}}$  given as in equation (1). In the subsequent development we will assume that  $X_{t,j} \in \mathbb{R}$ ,  $t = 1, \dots, T$ ,  $j = 1, \dots, p$ , are such that

$$\sum_{n \in \mathbb{N}_0} \delta(n,d) (\mathbf{X}^T \mathbf{\Lambda}_n^{-1} \mathbf{X})^{-1} < \infty. \quad (14)$$

Note that under conditions in Theorem 4 in [16] and Lemma 1, from Cauchy-Schwartz inequality,

$$\sum_{n \in \mathbb{N}_0} \delta(n,d) \mathbf{\Lambda}_n < \infty.$$



The GLS functional parameter estimator of  $\boldsymbol{\beta} = [\beta_1, \beta_2, \dots, \beta_p]^T$  is computed from projection into the orthonormal basis  $\{S_{n,j}^d, j = 1, \dots, \delta(n, d), n \in \mathbb{N}_0\}$  of eigenfunctions of the Laplace Beltrami operator  $\Delta_d$  on  $L^2(\mathbb{M}_d, d\nu, \mathbb{R})$ . Specifically, from equations (11)–(12), the GLS  $\hat{\boldsymbol{\beta}}$  is the minimizer of the mean quadratic loss function

$$\begin{aligned} L &= \left\| \tilde{\mathbf{Y}} - \mathbf{X}\boldsymbol{\beta} \right\|_{\mathbf{R}_{\tilde{\boldsymbol{\varepsilon}}\tilde{\boldsymbol{\varepsilon}}}^{-1}} = \sum_{n \in \mathbb{N}_0} \sum_{j=1}^{\delta(n,d)} \left[ \tilde{\mathbf{Y}}_{n,j} - \mathbf{X}\boldsymbol{\beta}_{n,j} \right]^T \boldsymbol{\Lambda}_n^{-1} \left[ \tilde{\mathbf{Y}}_{n,j} - \mathbf{X}\boldsymbol{\beta}_{n,j} \right] \\ &= \sum_{n \in \mathbb{N}_0} \sum_{j=1}^{\delta(n,d)} \|\tilde{\boldsymbol{\varepsilon}}_{n,j}\|_{\boldsymbol{\Lambda}_n^{-1}}^2, \end{aligned} \quad (15)$$

where, as before,  $\mathbf{X} = (X_{t,h})_{t=1,\dots,T;h=1,\dots,p}$ , and for  $n \in \mathbb{N}_0$  and  $j = 1, \dots, \delta(n, d)$ ,

$$\begin{aligned} \boldsymbol{\beta}_{n,j} &= \left( \beta_{n,j}^{(1)}, \dots, \beta_{n,j}^{(p)} \right)^T \\ \tilde{\mathbf{Y}}_{n,j} &= \left( \tilde{Y}_{n,j}(1), \dots, \tilde{Y}_{n,j}(T) \right)^T \\ \tilde{\boldsymbol{\varepsilon}}_{n,j} &= \left( \left\langle \tilde{\boldsymbol{\varepsilon}}_1, S_{n,j}^d \right\rangle_{L^2(\mathbb{M}_d, d\nu, \mathbb{R})}, \dots, \left\langle \tilde{\boldsymbol{\varepsilon}}_T, S_{n,j}^d \right\rangle_{L^2(\mathbb{M}_d, d\nu, \mathbb{R})} \right)^T. \end{aligned}$$

Here, for each  $n \in \mathbb{N}_0$ ,  $\boldsymbol{\Lambda}_n^{-1}$  denotes the matrix defining the bilinear form characterizing the inner product of the Reproducing Kernel Hilbert Space (RKHS) of  $(\tilde{\boldsymbol{\varepsilon}}_{n,j}, j = 1, \dots, \delta(n, d))$ . Hence,

$$\hat{\boldsymbol{\beta}}_{n,j} = (\mathbf{X}^T \boldsymbol{\Lambda}_n^{-1} \mathbf{X})^{-1} \mathbf{X}^T \boldsymbol{\Lambda}_n^{-1} \tilde{\mathbf{Y}}_{n,j}, \quad j = 1, \dots, \delta(n, d), \quad n \in \mathbb{N}_0. \quad (16)$$

Thus, our predictor of the response is given by:

$$\hat{\mathbf{Y}}(\mathbf{x}) = \mathbf{H} \left( \mathbf{X}(\hat{\boldsymbol{\beta}}) \right) (\mathbf{x}), \quad \mathbf{x} \in \mathbb{M}_d, \quad (17)$$

where, for  $\mathbf{x} \in \mathbb{M}_d$ ,

$$\begin{aligned} \hat{\boldsymbol{\beta}}(\mathbf{x}) &= \sum_{n \in \mathbb{N}_0} \sum_{j=1}^{\delta(n,d)} \hat{\boldsymbol{\beta}}_{n,j} S_{n,j}^d(\mathbf{x}) \\ &= \left( \sum_{n \in \mathbb{N}_0} \sum_{j=1}^{\delta(n,d)} \hat{\boldsymbol{\beta}}_{n,j}^{(1)} S_{n,j}^d(\mathbf{x}), \dots, \sum_{n \in \mathbb{N}_0} \sum_{j=1}^{\delta(n,d)} \hat{\boldsymbol{\beta}}_{n,j}^{(p)} S_{n,j}^d(\mathbf{x}) \right)^T. \end{aligned} \quad (18)$$

### 3.2 Second-order moments of the GLS functional parameter estimator

The following proposition provides the functional second-order moments of the unbiased GLS parameter estimator of  $\boldsymbol{\beta}$  computed in (18).

**Proposition 1** *The following identities hold:*

- (i)  $E[\hat{\beta}_{n,j}] = \beta_{n,j}$ ,  $j = 1, \dots, \delta(n, d)$ ,  $n \in \mathbb{N}_0$ , i.e.,  $E[\hat{\beta}] = \beta$ .
- (ii)  $\text{Var}[\hat{\beta}_{n,j}] = (\mathbf{X}^T \Lambda_n^{-1} \mathbf{X})^{-1}$ ,  $j = 1, \dots, \delta(n, d)$ ,  $n \in \mathbb{N}_0$ , i.e.,  
 $\text{Var}(\hat{\beta}) = \sum_{n \in \mathbb{N}_0} \delta(n, d) (\mathbf{X}^T \Lambda_n^{-1} \mathbf{X})^{-1}$ , where  $\mathbf{X}$  has been introduced in equation (10).

**Proof.**

The proof of (i) and (ii) follows straightforward as in the real-valued case. Specifically,

$$\begin{aligned}
E[\hat{\beta}_{n,j}] &= E\left[(\mathbf{X}^T \Lambda_n^{-1} \mathbf{X})^{-1} \mathbf{X}^T \Lambda_n^{-1} \tilde{\mathbf{Y}}_{n,j}\right] \\
&= (\mathbf{X}^T \Lambda_n^{-1} \mathbf{X})^{-1} \mathbf{X}^T \Lambda_n^{-1} E[\tilde{\mathbf{Y}}_{n,j}] \\
&= (\mathbf{X}^T \Lambda_n^{-1} \mathbf{X})^{-1} \mathbf{X}^T \Lambda_n^{-1} \mathbf{X} \beta_{n,j} \\
&= \beta_{n,j}, \quad j = 1, \dots, \delta(n, d), \quad n \in \mathbb{N}_0.
\end{aligned} \tag{19}$$

Hence, from (19), for every  $\mathbf{x} \in \mathbb{M}_d$ ,

$$\begin{aligned}
E[\hat{\beta}(\mathbf{x})] &= E\left[\left(\sum_{n=0}^{\infty} \sum_{k=1}^{\delta(n,d)} \hat{\beta}_{n,k}^{(1)} S_{n,k}^d(\mathbf{x}), \dots, \sum_{n=0}^{\infty} \sum_{k=1}^{\delta(n,d)} \hat{\beta}_{n,k}^{(p)} S_{n,k}^d(\mathbf{x})\right)^T\right] \\
&= \left(\sum_{n=0}^{\infty} \sum_{k=1}^{\delta(n,d)} E[\hat{\beta}_{n,k}^{(1)}] S_{n,k}^d(\mathbf{x}), \dots, \sum_{n=0}^{\infty} \sum_{k=1}^{\delta(n,d)} E[\hat{\beta}_{n,k}^{(p)}] S_{n,k}^d(\mathbf{x})\right)^T \\
&= \left(\sum_{n=0}^{\infty} \sum_{k=1}^{\delta(n,d)} \beta_{n,k}^{(1)} S_{n,k}^d(\mathbf{x}), \dots, \sum_{n=0}^{\infty} \sum_{k=1}^{\delta(n,d)} \beta_{n,k}^{(p)} S_{n,k}^d(\mathbf{x})\right)^T = \beta(\mathbf{x}).
\end{aligned} \tag{20}$$

Regarding (ii), as it is well known, since for every  $j = 1, \dots, \delta(n, d)$ ,  $n \in \mathbb{N}_0$ ,

$$\hat{\beta}_{n,j} = \beta_{n,j} + (\mathbf{X}^T \Lambda_n^{-1} \mathbf{X})^{-1} \mathbf{X}^T \Lambda_n^{-1} \tilde{\epsilon}_{n,j}, \tag{21}$$

we have

$$\begin{aligned}
\text{Var}[\hat{\beta}_{n,j}] &= E\left[\left(\hat{\beta}_{n,j} - \beta_{n,j}\right)^T \left(\hat{\beta}_{n,j} - \beta_{n,j}\right)\right] \\
&= (\mathbf{X}^T \Lambda_n^{-1} \mathbf{X})^{-1} \mathbf{X}^T \Lambda_n^{-1} \Lambda_n \Lambda_n^{-1} \mathbf{X} (\mathbf{X}^T \Lambda_n^{-1} \mathbf{X})^{-1} \\
&= (\mathbf{X}^T \Lambda_n^{-1} \mathbf{X})^{-1}, \quad \forall j \in \{1, \dots, \delta(n, d)\}, \quad n \in \mathbb{N}_0.
\end{aligned} \tag{22}$$

From (22), applying uncorrelation of the sequence of centered random processes  $\{\tilde{\varepsilon}_{n,j}(t), t \in [0, T]\}$  (see equation 21)

$$E \left[ \left\| \hat{\boldsymbol{\beta}} - \boldsymbol{\beta} \right\|_{L^2(\mathbb{M}_d, d\nu, \mathbb{R})}^2 \right] = \sum_{n \in \mathbb{N}_0} \delta(n, d) (\mathbf{X}^T \boldsymbol{\Lambda}_n^{-1} \mathbf{X})^{-1},$$

under condition (14).

### 3.3 Functional spectral based plug-in estimation of $\boldsymbol{\beta}$

This section presents a plug-in GLS estimation methodology when the second order structure of the error term is unknown. In our case, the entries of the matrix sequence  $\{\boldsymbol{\Lambda}_n, n \in \mathbb{N}_0\}$  are misspecified. The approach presented is based on the estimation of such entries in the spectral domain under the following semiparametric modeling in the spectral domain (see [24]):

**Assumption I.** Assume that the entries  $f_n, n \in \mathbb{N}_0$ , of matrix sequence in (13) admit the following semiparametric modeling, for every  $n \in \mathbb{N}_0$ ,

$$f_{n,\theta}(\omega) = B_n^\eta(0) M_n(\omega) [4(\sin(\omega/2))^2]^{-\alpha(n,\theta)/2}, \quad \theta \in \Theta, \quad \omega \in [-\pi, \pi] \quad (23)$$

where  $\alpha(n, \theta)$ ,  $M_n(\omega)$ , and  $B_n^\eta(0)$  are the eigenvalues of the LRD operator  $\mathcal{A}_\theta$ , of the Hilbert–Schmidt operator spectral family  $\{\mathcal{M}_\omega, \omega \in [-\pi, \pi]\}$ , and of the autocovariance operator  $R_0^\eta$  of the manifold white noise innovation process  $\eta$  involved in the definition of the error term  $\varepsilon$ , respectively. Note that in our simulations in Section 4 we have considered the case where the regular spectral operator family  $\{\mathcal{M}_\omega, \omega \in [-\pi, \pi]\}$  corresponds to SRD in the case where  $\alpha(n, \theta) = 0$ , for every  $n \in \mathbb{N}_0$ , and  $\theta \in \Theta$ .

We apply the minimum contrast estimation strategy introduced in equations (5.1)–(5.19) in [24], and equations (3.8)–(3.16) in [18], for the special case of  $H = L^2(\mathbb{M}_d, d\nu, \mathbb{C})$ . Specifically, parameter  $\theta$  in equation (23), characterizing the pure point spectrum of LRD operator  $\mathcal{A}_\theta$ , is estimated by  $\hat{\theta}_T$  satisfying

$$\hat{\theta}_T = \arg \min_{\theta \in \Theta} \left\| - \int_{-\pi}^{\pi} p_\omega^{(T)} \ln(\Upsilon_{\omega,\theta}) \mathcal{W}_\omega d\omega \right\|_{\mathcal{L}(L^2(\mathbb{M}_d, d\nu; \mathbb{C}))}, \quad (24)$$

where for each  $\theta \in \Theta$ , and  $\omega \in [-\pi, \pi]$ ,  $\omega \neq 0$ ,

$$\Upsilon_{\omega,\theta} = [\mathcal{N}_\theta]^{-1} \mathcal{F}_{\omega,\theta} = \mathcal{F}_{\omega,\theta} [\mathcal{N}_\theta]^{-1}, \quad (25)$$

with  $\{\mathcal{F}_{\omega,\theta}, \omega \in [-\pi, \pi]\}$  denoting the adopted semiparametric spectral density operator family model, and the integral operator  $\mathcal{N}_\theta$  has kernel

$$\mathcal{K}_{\mathcal{N}_\theta}(\mathbf{x}, \mathbf{y}) = \sum_{n \in \mathbb{N}_0} \widetilde{W}(n) \left[ \int_{-\pi}^{\pi} \frac{B_n^\eta(0) M_n(\omega) [4(\sin(\omega/2))^2]^{-\alpha(n,\theta)/2}}{|\omega|^{-\gamma}} d\omega \right]$$

$$\times \sum_{j=1}^{\delta(n,d)} S_{n,j}^d(\mathbf{x}) S_{n,j}^d(\mathbf{y}), \quad \mathbf{x}, \mathbf{y} \in \mathbb{M}_d, \quad \theta \in \Theta, \quad (26)$$

where  $\widetilde{W}$  denotes the positive self-adjoint operator on  $L^2(\mathbb{M}_d, d\nu, \mathbb{C})$  factorizing the weighting operator  $\mathcal{W}_\omega = \widetilde{W}|\omega|^\gamma$ , for every  $\omega \in [-\pi, \pi]$ , and  $\gamma > 0$ . Fourier transform inversion formula leads to the corresponding estimation

$$\widehat{B}_{n,\widehat{\theta}_T}(t) = \int_{-\pi}^{\pi} \exp(i\omega t) f_{n,\widehat{\theta}_T}(\omega) d\omega, \quad n \in \mathbb{N}_0,$$

of the entries of  $\Lambda_{n,\widehat{\theta}_T}$ , given by

$$\Lambda_{n,\widehat{\theta}_T} = \left( \begin{bmatrix} \widehat{B}_{n,\widehat{\theta}_T}(0) & \cdots & \widehat{B}_{n,\widehat{\theta}_T}(T-1) \\ \vdots & \ddots & \vdots \\ \widehat{B}_{n,\widehat{\theta}_T}(T-1) & \cdots & \widehat{B}_{n,\widehat{\theta}_T}(0) \end{bmatrix} \right), \quad n \in \mathbb{N}_0.$$

Thus, for every  $n \in \mathbb{N}_0$ ,

$$\widehat{\beta}_{n,j,\widehat{\theta}_T} = \left( \mathbf{X}^T \Lambda_{n,\widehat{\theta}_T}^{-1} \mathbf{X} \right)^{-1} \mathbf{X}^T \Lambda_{n,\widehat{\theta}_T}^{-1} \widetilde{\mathbf{Y}}_{n,j}, \quad n \in \mathbb{N}_0, \quad j = 1, \dots, \delta(n,d),$$

and the corresponding plug-in nonlinear predictor is computed as

$$\widehat{\mathbf{Y}}_{\widehat{\theta}_T}(\mathbf{x}) = \mathbf{H} \left( \mathbf{X}(\widehat{\beta}_{\widehat{\theta}_T}) \right) (\mathbf{x}), \quad \forall \mathbf{x} \in \mathbb{M}_d, \quad (27)$$

where for  $\mathbf{x} \in \mathbb{M}_d$ ,

$$\begin{aligned} \widehat{\beta}_{\widehat{\theta}_T}(\mathbf{x}) &= \sum_{n \in \mathbb{N}_0} \sum_{j=1}^{\delta(n,d)} \widehat{\beta}_{n,j,\widehat{\theta}_T} S_{n,j}^d(\mathbf{x}) \\ &= \left( \sum_{n \in \mathbb{N}_0} \sum_{j=1}^{\delta(n,d)} \widehat{\beta}_{n,j,\widehat{\theta}_T}^{(1)} S_{n,j}^d(\mathbf{x}), \dots, \sum_{n \in \mathbb{N}_0} \sum_{j=1}^{\delta(n,d)} \widehat{\beta}_{n,j,\widehat{\theta}_T}^{(p)} S_{n,j}^d(\mathbf{x}) \right)^T. \end{aligned} \quad (28)$$

## 4 Simulations

This section considers the sphere as manifold to illustrate the performance of the multiple functional nonlinear regression predictor proposed (see Supplementary Material for the linear case corresponding to operator  $\mathbf{H}$  being the identity operator). Specifically, we consider the case where  $\mathbf{H}(X\beta)(\mathbf{x}) = \exp(X\beta)(\mathbf{x}) = \sum_{k=0}^{\infty} \frac{(X\beta(\mathbf{x}))^k}{k!}$ , with  $(X\beta(\mathbf{x}))^k$  being the  $T$ -dimensional vector with components  $(\sum_{j=1}^p X_{t,j}\beta_j(\mathbf{x}))^k$ ,  $t = 1, \dots, T$ , for every  $\mathbf{x} \in \mathbb{M}_d$ , and  $k \in \mathbb{N}_0$ . The regression predictors (17) and (27) are then implemented in Sections 4.1 and 4.2, respectively, under a log-Gaussian scenario in terms of spherical harmonics.

## 4.1 Theoretical predictor

As commented before, this section illustrates the performance of the nonlinear regression predictor (17) for the case of  $\mathbf{H}(\mathbf{X}(\beta)) = \exp(\mathbf{X}(\beta))$ , when the error term  $\varepsilon$  is a log-gaussian isotropic spherical functional process displaying spherical scale varying LRD in time. The regression prediction results are tested for functional sample sizes  $T = 110, 300, 500$ . A wavelet-based simulation of fractional Brownian motion with Hurst parameters  $H = 0.5/k$ ,  $k = 1, 2$ , is applied in the definition of the temporal dynamics of the covariates at each one of the two spherical scales selected. Specifically, our choice of the spherical functional regression parameters is given by the eigenfunctions  $S_{1,1}^2$ , and  $S_{1,2}^2$  of the spherical Laplace Beltrami operator, displayed at the two plots of the first line of Figure 18 in Section 2.1 of the Supplementary Material. The regression error is generated from its truncated expansion (see Figure 19 in Section 2.1 of the Supplementary Material, where realization 75 is showed), obtained from its projection into the eight eigenfunctions plotted in Figure 18 of Section 2.1 of the Supplementary Material. The corresponding time varying coefficients are computed from the inverse Fourier transform of the frequency varying eigenvalues of the square root of the semiparametric spectral density operator family in equation (23) under **Assumption I** (see Figure 1).

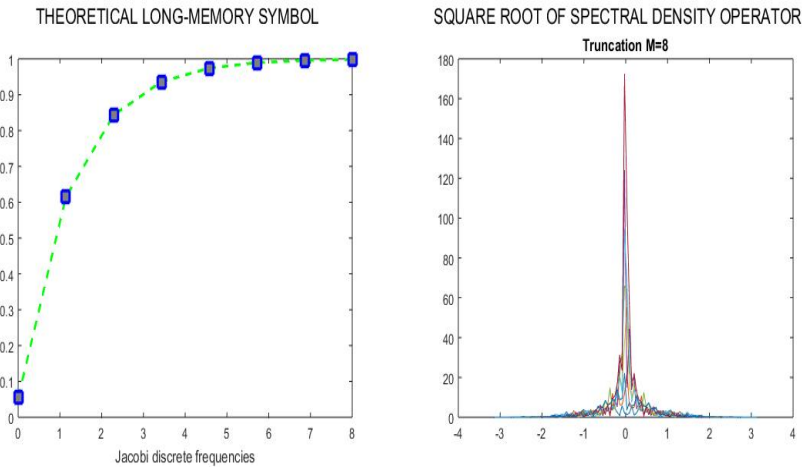


Figure 1: LRD operator eigenvalues (left-hand side), and the squared root of frequency varying eigenvalues in 50th realization, for the first 8 Laplace Beltrami operator eigenspaces selected (right-hand side)

The nonlinear response is estimated from equation (17), approximated by the nonlinear transformation of the corresponding truncated version of the GLS linear predictor. See Figures 2 and 3, where one realization of the nonlinear response and its functional regression prediction are displayed, respectively. Our

empirical analysis is based on the simulation of  $R = 100$  repetitions of the spherical functional samples. Specifically, we compute the empirical mean absolute errors associated with the theoretical spherical functional regression predictor for the functional sample sizes  $T = 110, 300$  (see Figures 20 and 21 in Section 2.1 of the Supplementary Material), and for  $T = 500$  (see Figure 4). One can observe an important reduction of such empirical mean absolute errors as the functional sample size increases.

In the next section, under a misspecified model scenario, the residual analysis achieved is performed in the functional spectral domain, implementing the minimum contrast estimation of the second-order structure of the log-error term displaying spatial scale varying LRD, considering the case of an increasing sequence of LRD operator eigenvalues (see Figure 1 where these eigenvalues are plotted for the eight spherical scales analyzed). The case of a decreasing sequence of LRD eigenvalues can be seen in Section 2.2.1 of the Supplementary Material.

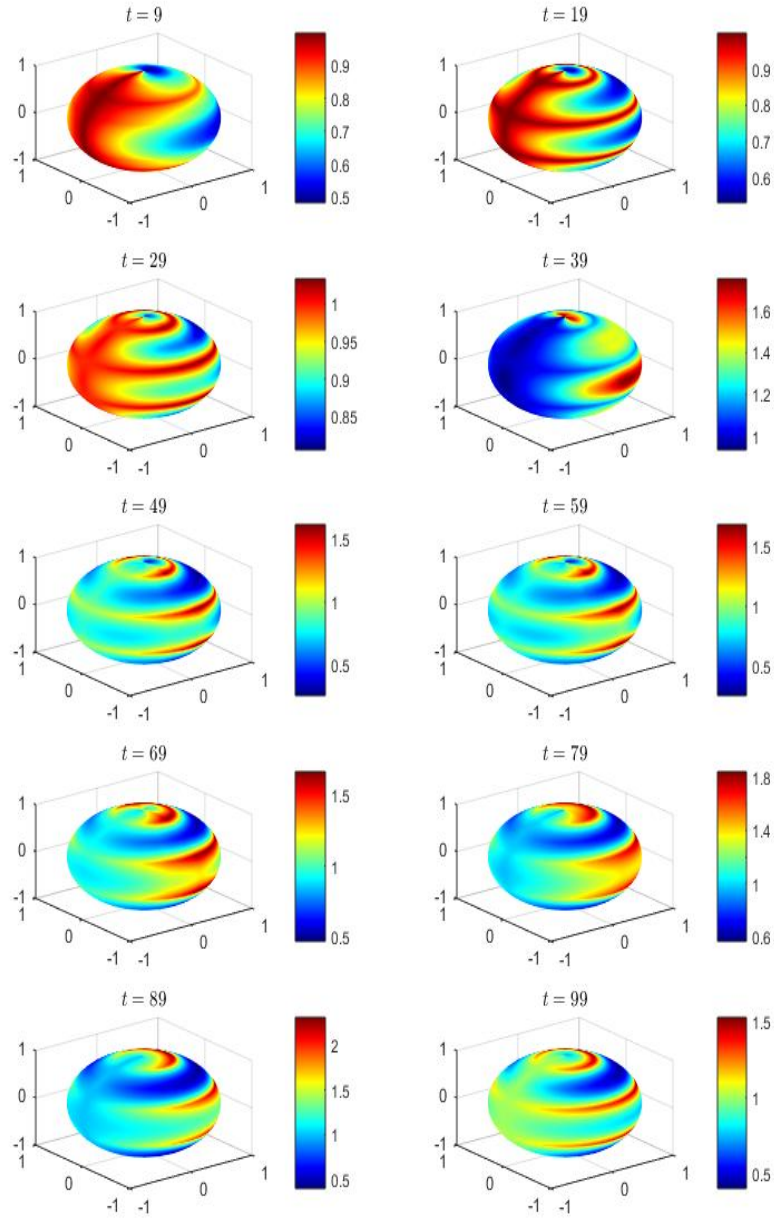


Figure 2: Log-Gaussian nonlinear spherical functional response values at times  $t = 9, 19, 29, 39, 49, 59, 69, 79, 89, 99$  (corresponding to realization 75)

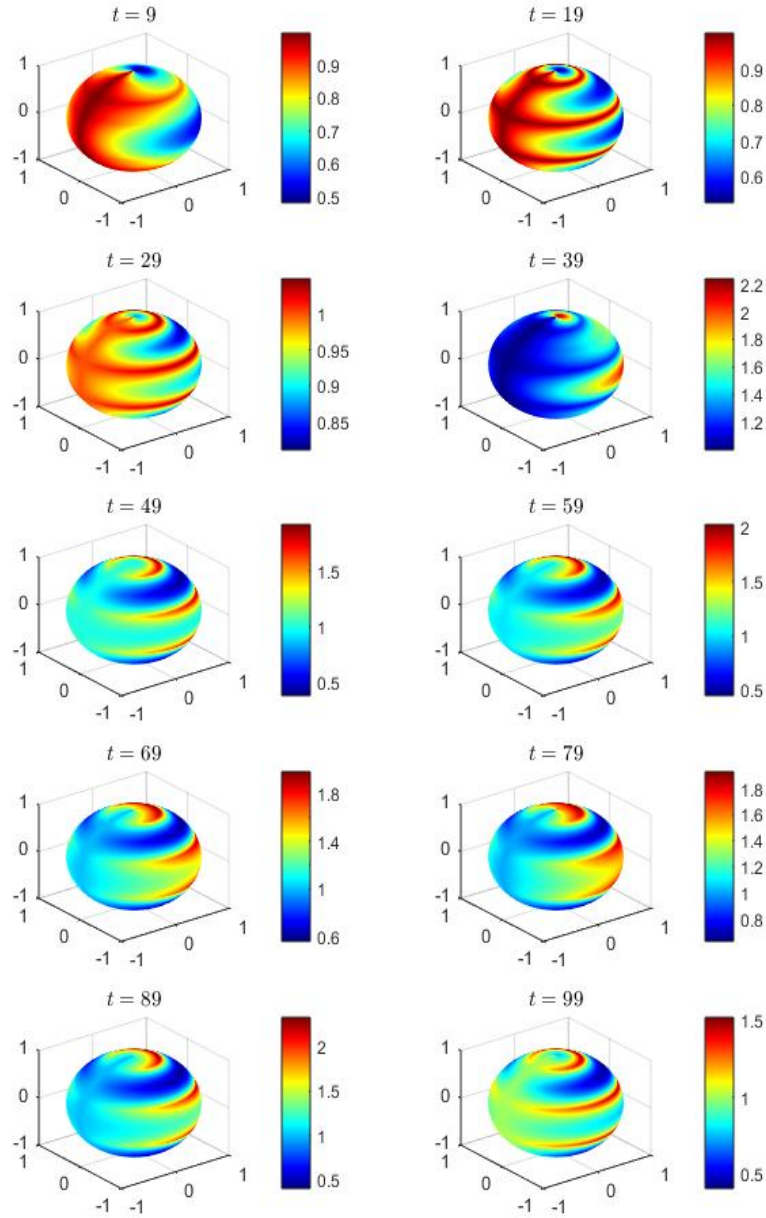


Figure 3: Nonlinear spherical functional response predictions at times  $t = 9, 19, 29, 39, 49, 59, 69, 79, 89, 99$  (corresponding to realization 75)



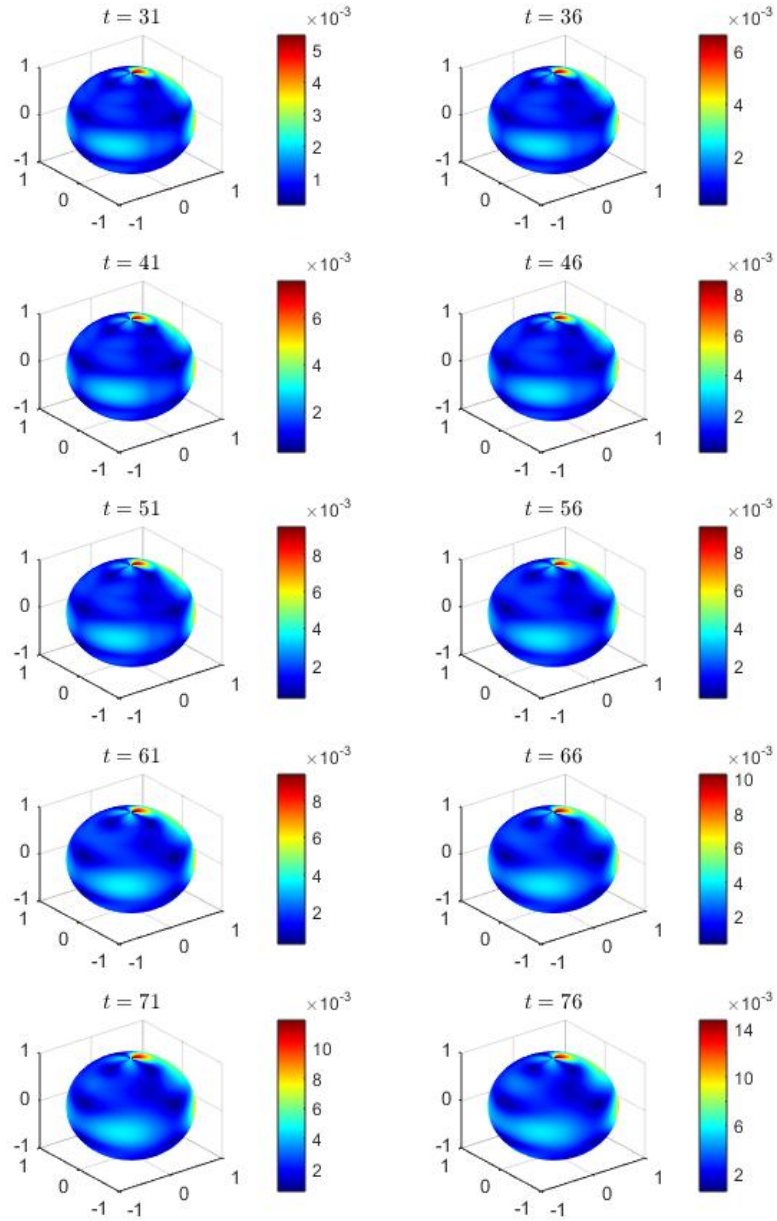


Figure 4: Empirical mean absolute errors, based on 100 repetitions, for functional sample size  $T = 500$ , associated with the spherical functional regression predictor at times  $t = 31, 36, 41, 46, 51, 56, 61, 66, 71, 76$

## 4.2 Plug-in predictor

In this section, in the generation of the temporal covariates the Hurst parameter value  $H = 0.001$  has been considered in the wavelet-based approximation of fractional Brownian motion. Our choice here of the spherical functional regression parameters corresponds to the eigenfunctions  $S_{1,1}^2$ , and  $S_{2,1}^2$  plotted at the left-hand side of the first two lines of Figure 18 in Section 2.1 of the Supplementary Material.

Specifically, since we assume that the second-order structure of the LRD isotropic spherical functional error term is unknown, we apply minimum contrast estimation in the functional spectral domain to compute a second-order approximation of the Gaussian log-error term. In the implementation of this estimation technique (see [18]; [24]), we consider a set of 100 candidates for the first eight eigenvalues of the LRD operator (see Figure 22 in Section 2.2 in the Supplementary Material).

The 50th realization of the spherical functional error term, and its spectral based minimum contrast estimation are plotted in Figures 23 and 24 in Section 2.2 of the Supplementary Material, respectively. The corresponding empirical mean absolute errors, based on 100 repetitions (see Figure 25 in Section 2.2 of the Supplementary Material), and based on 500 repetitions (see Figure 5), associated with the minimum contrast estimator of the spherical error term are computed. One can observe changes in the spatial patterns improving the accuracy when the number of repetitions increases from 100 to 500. Furthermore, there is an important reduction of the spatial areas with the highest magnitudes of these empirical mean absolute errors.

The plug-in regression spherical functional predictor, in the linearized model, of the response is then obtained. The corresponding empirical mean absolute errors in the nonlinear prediction of the response are also computed as showed for  $R = 100$  in Figure 26 in Section 2.2 of the Supplementary Material, and for  $R = 500$  in Figure 8. One can observe the decrease of the magnitude in some temporal nodes as  $R$  increases. Additionally, the variation in the spatial patterns suggests an improvement in the estimation provided by the plug-in regression spherical functional predictor when the number of repetitions goes from 100 to 500. The spherical functional response values and their corresponding nonlinear response predictions in the 50th generation are previously given in Figures 6 and 7, respectively. See Section 2.2.1 of the Supplementary Material, where similar results are plotted for the case of a decreasing eigenvalue sequence of the LRD operator, characterizing the functional spectrum of the isotropic spherical functional error term.

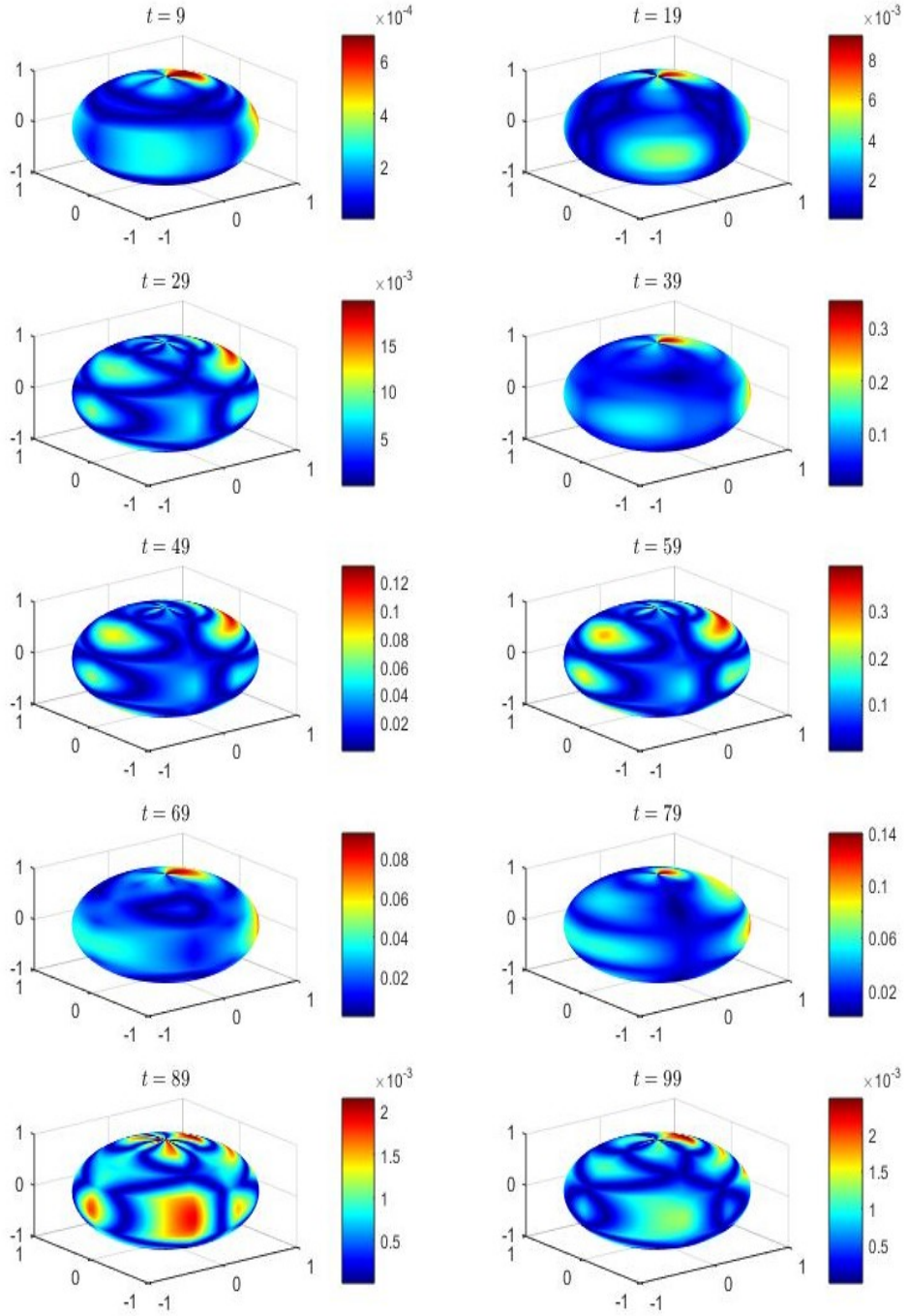


Figure 5: Empirical mean absolute errors, based on 500 repetitions, associated with the minimum contrast estimator of the spherical functional error term at times  $t = 9, 19, 29, 39, 49, 59, 69, 79, 89, 99$

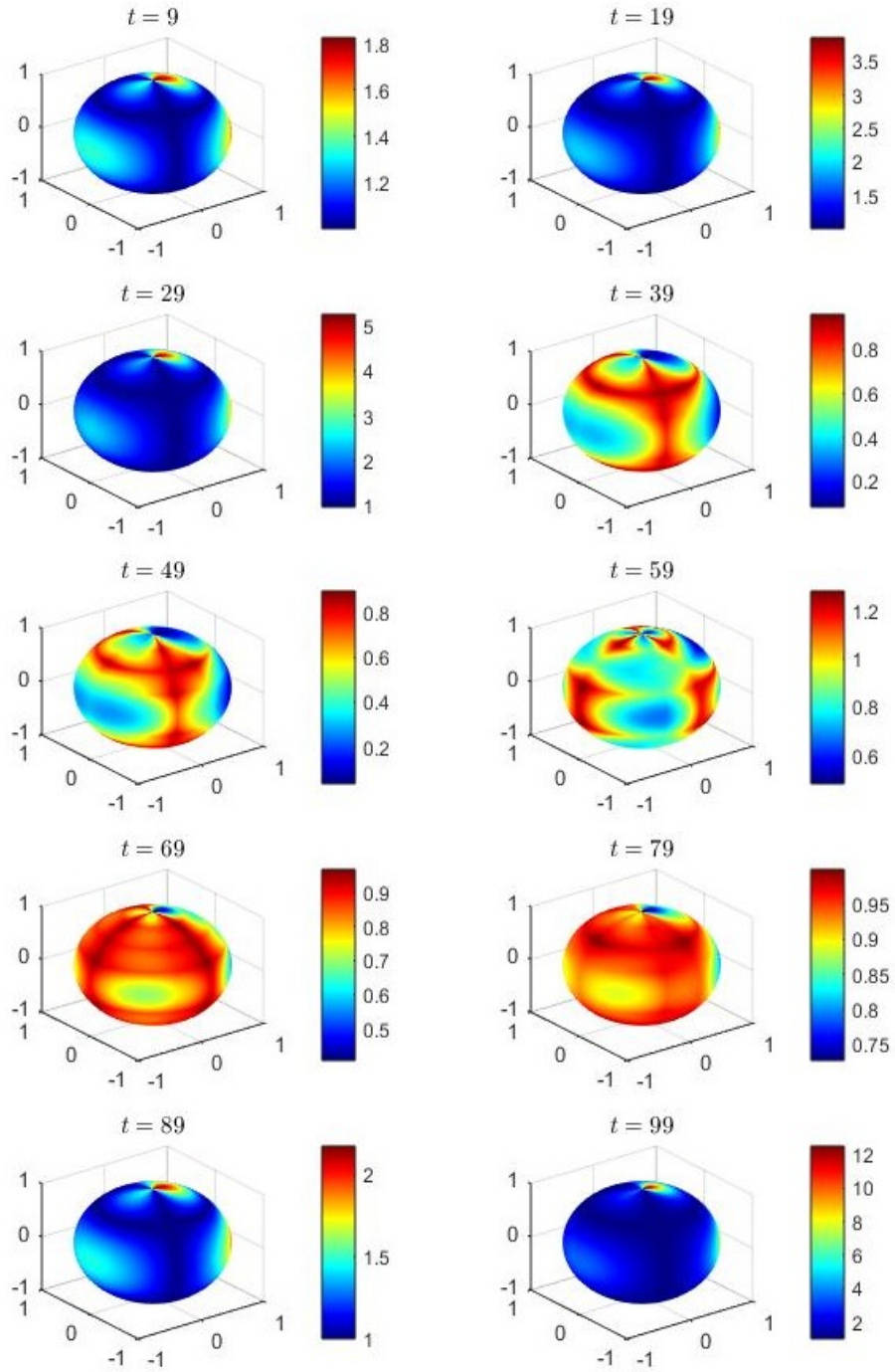


Figure 6: Nonlinear (log-Gaussian) spherical functional response values at times  $t = 9, 19, 29, 39, 49, 59, 69, 79, 89, 99$  (corresponding to realization 50)

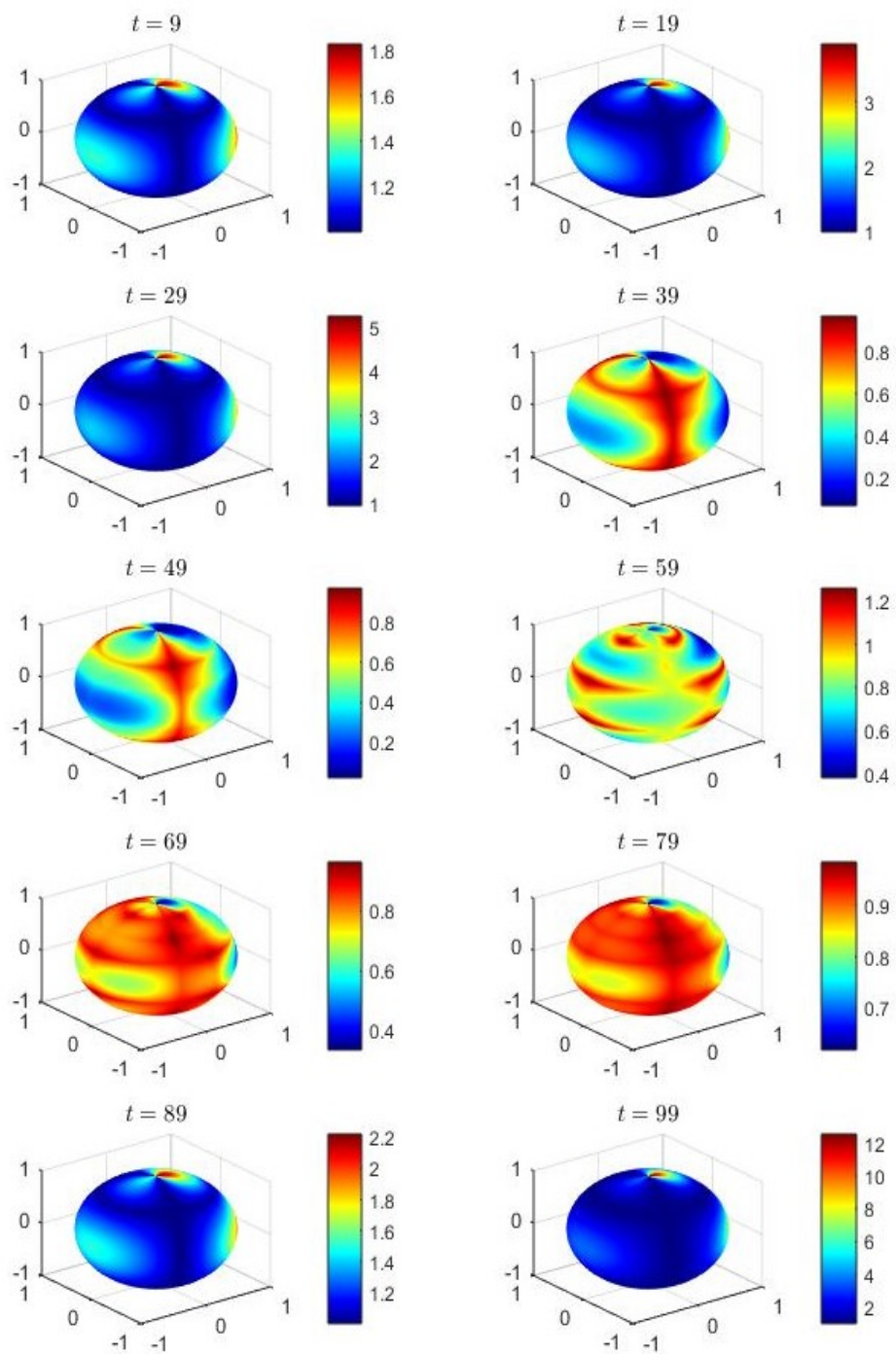


Figure 7: Nonlinear (log-Gaussian) spherical functional response regression predictions at times  $t = 9, 19, 29, 39, 49, 59, 69, 79, 89, 99$  (corresponding to realization 50)

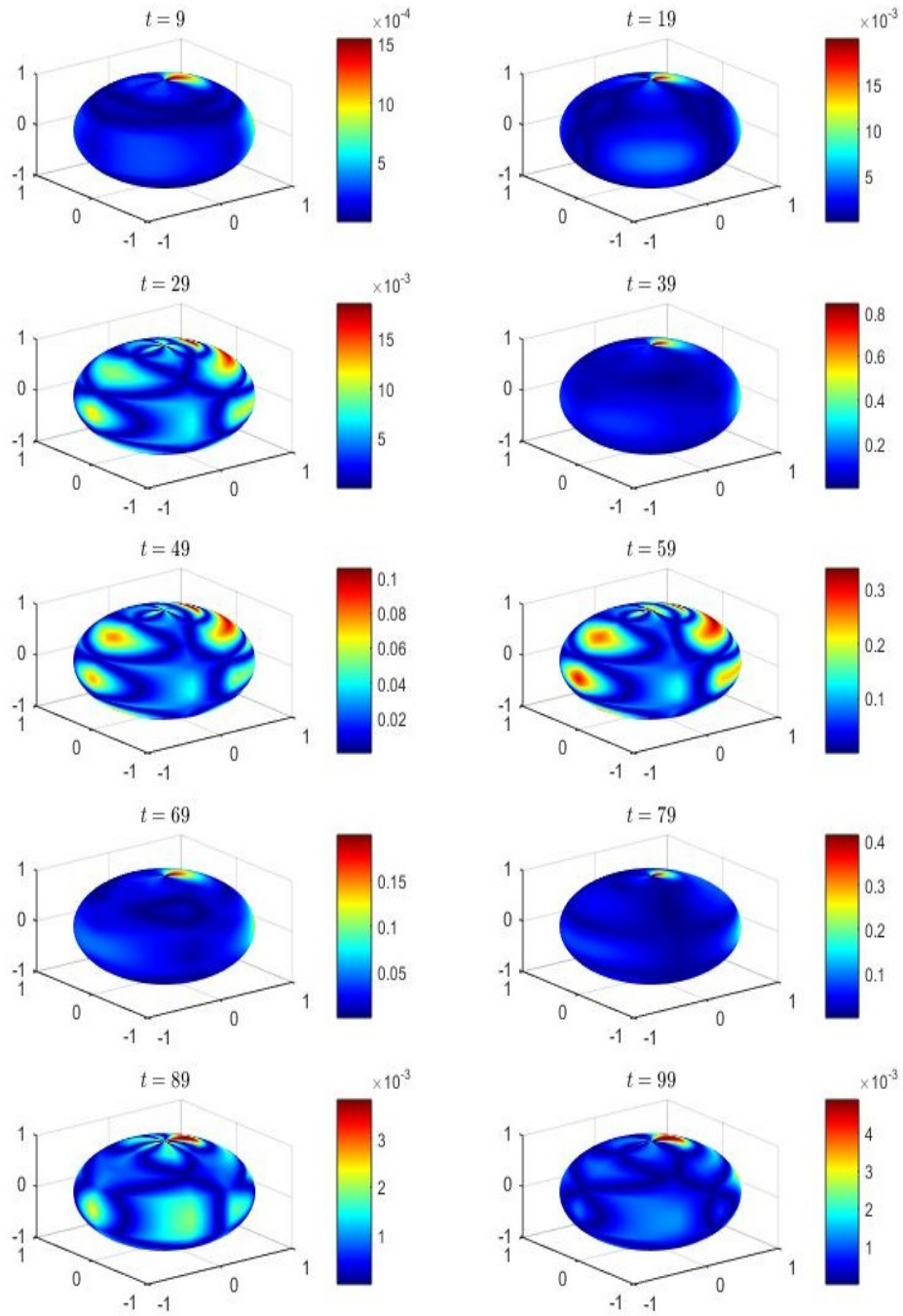


Figure 8: Empirical mean absolute errors, based on 500 repetitions, associated with the spherical functional nonlinear regression predictor at times  $t = 9, 19, 29, 39, 49, 59, 69, 79, 89, 99$

## 5 Real–data application

This section considers the implementation of the proposed nonlinear spherical functional regression methodology in the prediction of the time evolution of downward solar radiation flux earth maps, from the daily observation on the earth globe of atmospheric pressure at high cloud bottom. A synthetic data set is generated based on the nonlinear physical models governing both magnitudes, downward solar radiation flux and atmospheric pressure at high cloud bottom.

In the generations of spherical functional observations of downward solar radiation flux through autumn–winter, its nonlinear mean displayed in Figure 9 is computed after some steps involving several geophysical magnitudes. Specifically, a starting polar and azimuthal angle grid is considered with 180 nodes in the intervals  $(0, \pi)$ , and  $(0, 2\pi)$ , respectively. A meshgrid is then constructed in the corresponding two–dimensional angle interval. The polar angle values are converted into latitudes in the computation of the Zenith Angle (ZA), that is one of the input variables of the physical equation defining Solar Irradiance (SI). Note that the ZA depends on the time of the year, and the declination through a suitable trigonometric equation. The declination is given by a sinusoidal function also depending on the day of the year. Other parameters involved in these previous physical equations are the Earth Radius  $ER = 6371000$  in meters, and the Solar Constant  $G_0 = 1361$  in  $W/m^2$ .

The solar irradiance is obtained from the Clear Sky Index (CSI=0.8) by using the relationship

$$SI = G_0(CSI)(\cos(ZA))/\pi. \quad (29)$$

Finally, to reflect persistent in time of SI random fluctuations during autumn–winter, a standardized LRD isotropic spherical functional process is generated as error term, scaling each marginal with the solar irradiance standard deviation value 160.2262 (see Figure 10).

The nonlinear mean of the atmospheric pressure is computed (see Figure 32 of the Supplementary Material for spring–summer period, and Figure 11 for autumn–winter period), from the barometric equation, involving sea level pressure  $P_0 = 1013.25$ , air molar mass  $M = 0.029$  in kilograms per mole, acceleration due gravity  $g = 9.81$  in  $m/s^2$ , ideal gas constant  $RC = 8.314$ , Kelvin temperature  $TT = 273 + 15$ , and usual range of heights at bottom of high cloud, where we have considered the height interval (6000, 12000) in meters. Thus, pressures  $pp$  obey the equation

$$pp = P_0(\exp(-M(g)(heights)/(RC(TT)))).$$

Again, a meshgrid is constructed from latitude and days to finally compute the daily values of the spherical functional isotropic regressor mean over a year from the input argument  $pp$ , in terms of polar angle, amplitude of pressure variation with latitude and over days, and angular frequency corresponding to

an annual cycle. We have considered the value 49.6453 of pressure standard deviation in the normalization of each marginal of the spatiotemporal pressure process generated (see Figure 12), by adding to the computed nonlinear mean a standardized LRD isotropic spherical functional error term (see Figure 13).

Note that although this synthetic spherical functional data set has been generated for the time period of one year, for illustration purposes, we have restricted our attention to the period autumn–winter, where low pressure is frequently observed at earth globe areas of medium and high latitudes in both hemispheres, while the highest pressures are localized at tropical and subtropical areas. The reverse situation corresponds to the spring–summer period (see Figure 32 in Section 3 of the Supplementary Material). Indeed, this fact constitutes one of our main motivations to include in this nonlinear spherical functional regression problem the temporal information. Specially, regarding time–varying covariates in this example, one can see how spherical patterns displayed by the spherical functional regressor change drastically in these two periods (autumn–winter and spring–summer), affecting in a very different way the response defined by solar irradiance.

The results after implementation of the proposed spherical functional nonlinear multiple regression predictor are showed in Figure 14 where the original values of the response are plotted at the left–hand side for different times while at the right–hand side the corresponding spherical functional regression predictor values are showed. Note that, the spherical functional regression predictor reproduces the magnitudes and the spherical patterns of the spherical functional solar irradiance very close.

The performance of the proposed regression prediction technique is illustrated by the implementation of 5–fold cross validation. The spherical functional 5–fold cross validation errors obtained by computing the proposed regression predictor are displayed in Figure 15. The absolute 5–fold cross validation errors associated with the plug–in predictor, after minimum contrast estimation of the error term are also plotted in Figure 16. Note that a slight difference between regression and plug–in regression performances is observed in the order of magnitude of the modulus of the 5–fold cross validation errors.



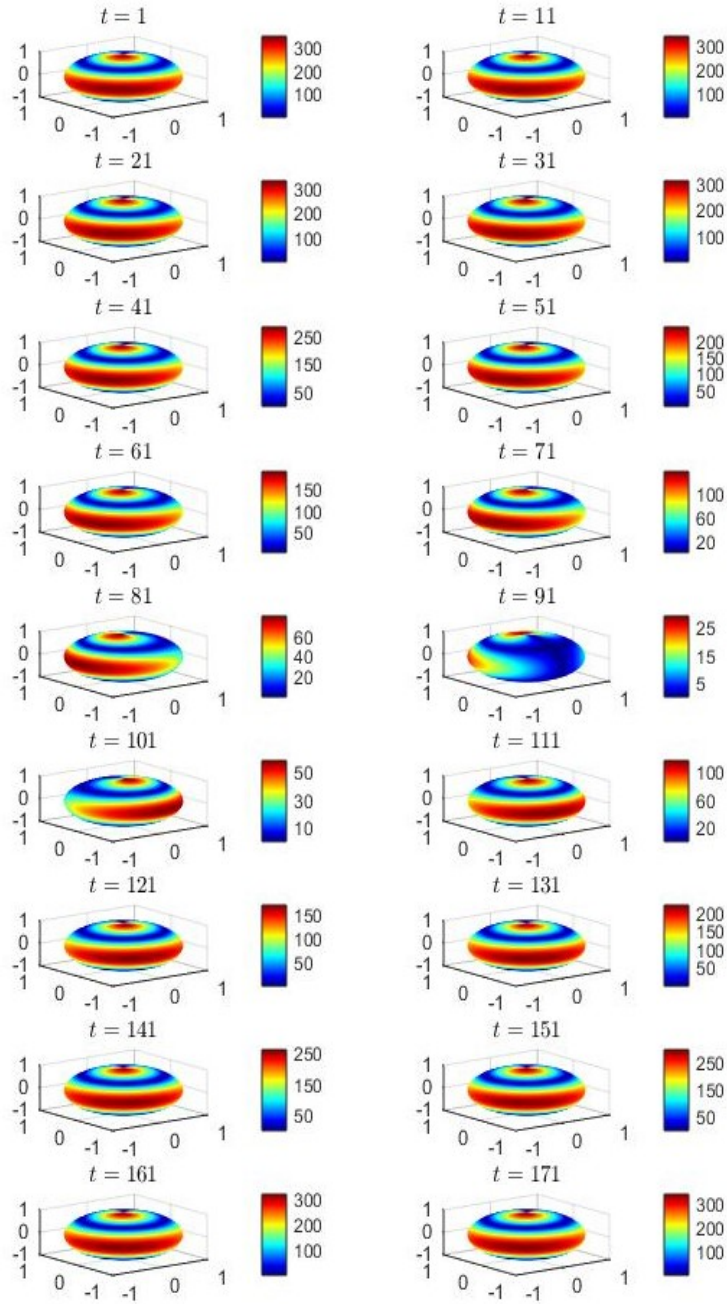


Figure 9: Nonlinear response mean computed from evaluation of physical model (29) of downward solar radiation flux during autumn-winter. Its spherical functional values are displayed at times  $t = 1, 11, 21, 31, 41, 51, 61, 71, 81, 91, 101, 111, 121, 131, 141, 151, 161, 171$

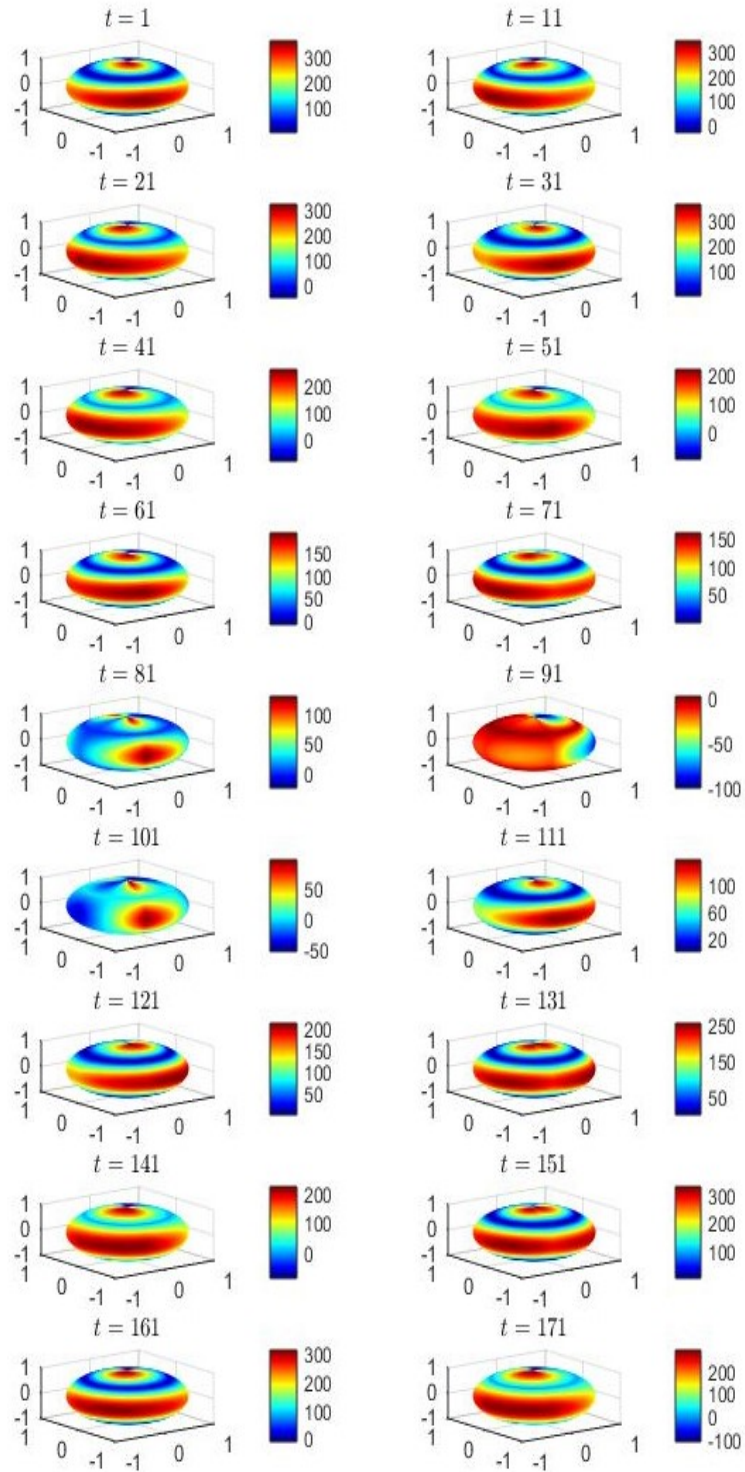


Figure 10: Daily spherical functional response observations during autumn-winter period. Generated synthetic data of downward solar radiation flux are displayed at times  $t = 1, 11, 21, 31, 41, 51, 61, 71, 81, 91, 101, 111, 121, 131, 141, 151, 161, 171$

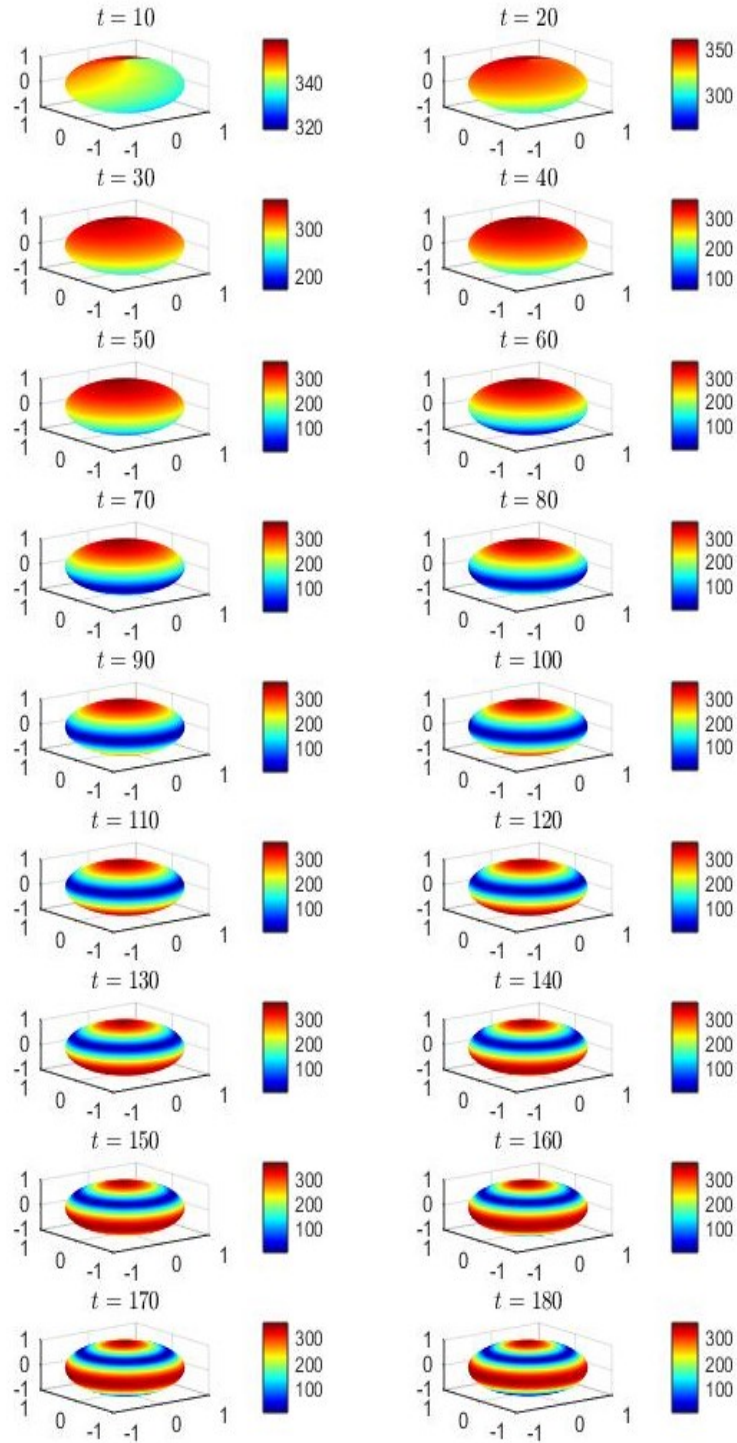


Figure 11: Nonlinear spherical functional regressor mean computed from barometric equation during autumn-winter. Its spherical functional values are displayed at times  $t = 10, 20, 30, 40, 50, 60, 70, 80, 90, 100, 110, 120, 130, 140, 150, 160, 170, 180$

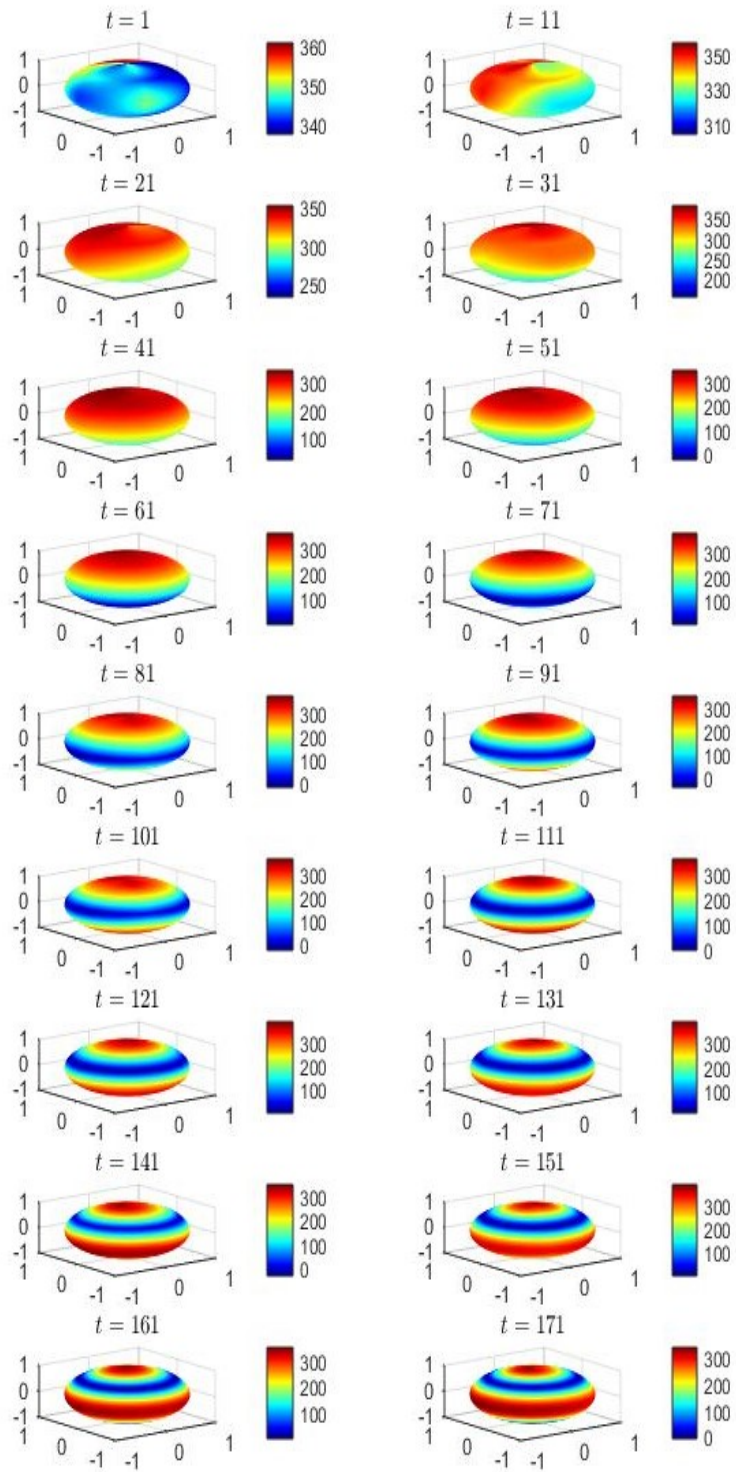


Figure 12: Daily spherical functional regressor observations during autumn-winter period. Generated synthetic data of atmospheric pressure at high cloud bottom are displayed at times  $t = 1, 11, 21, 31, 41, 51, 61, 71, 81, 91, 101, 111, 121, 131, 141, 151, 161, 171$

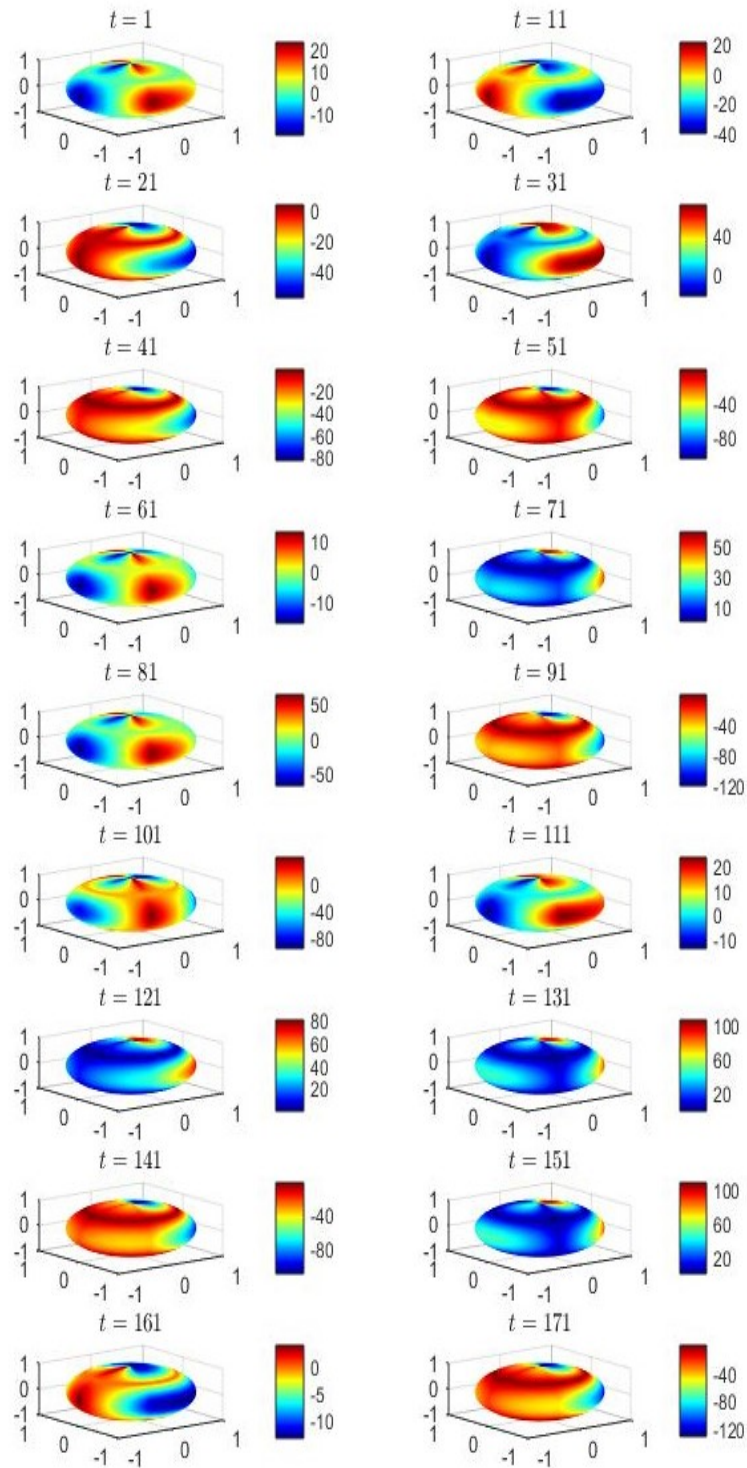


Figure 13: Spherical functional random effect at times  $t = 1, 11, 21, 31, 41, 51, 61, 71, 81, 91, 101, 111, 121, 131, 141, 151, 161, 171$

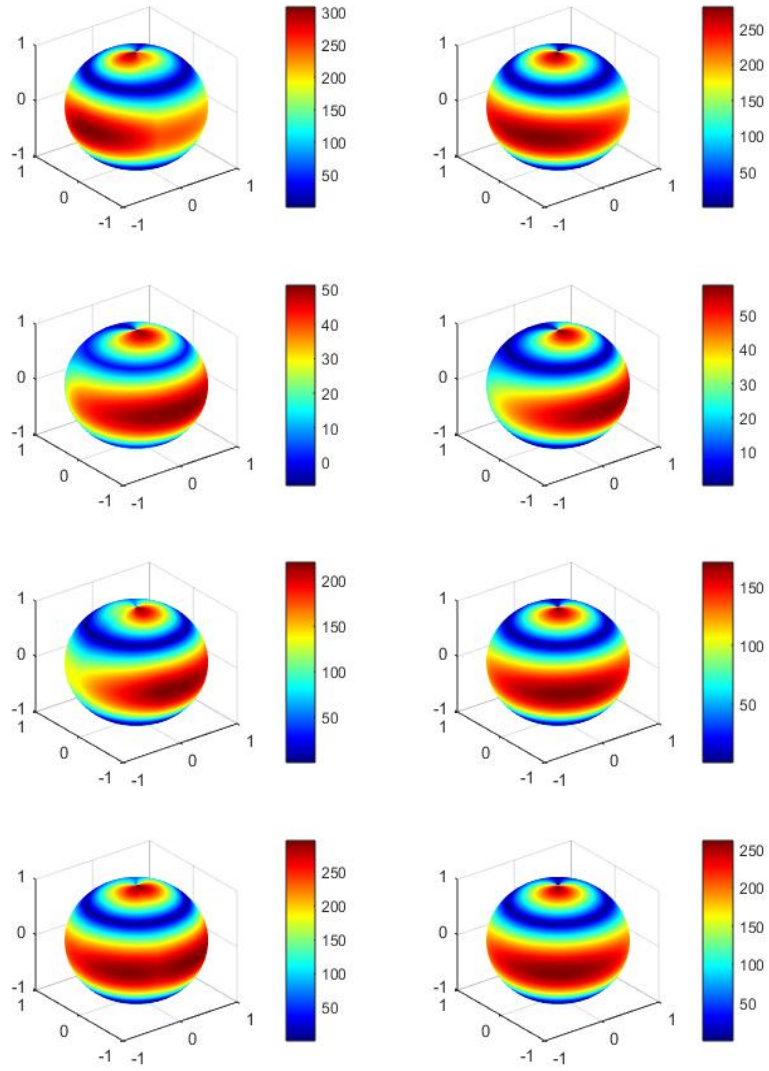


Figure 14: Spherical functional response values (left-hand side) and spherical functional regression prediction values (right-hand side) at times  $t = 41, 101, 121, 141$  from top to the bottom respectively

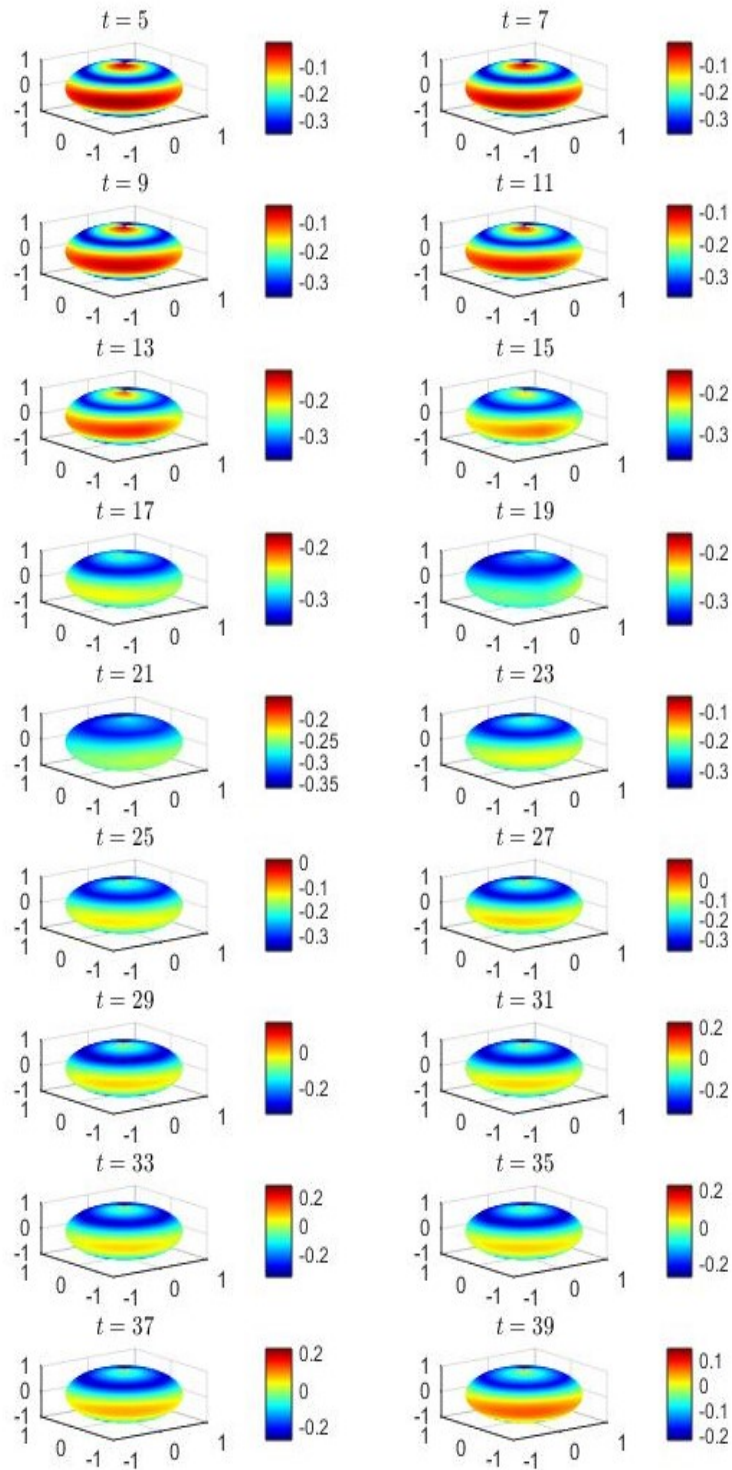


Figure 15: Spherical functional 5-fold-cross validation errors associated with response regression predictor. Their spherical functional values are displayed at times  $t = 5, 7, 9, 11, 13, 15, 17, 19, 21, 23, 25, 27, 29, 31, 33, 35, 37, 39$

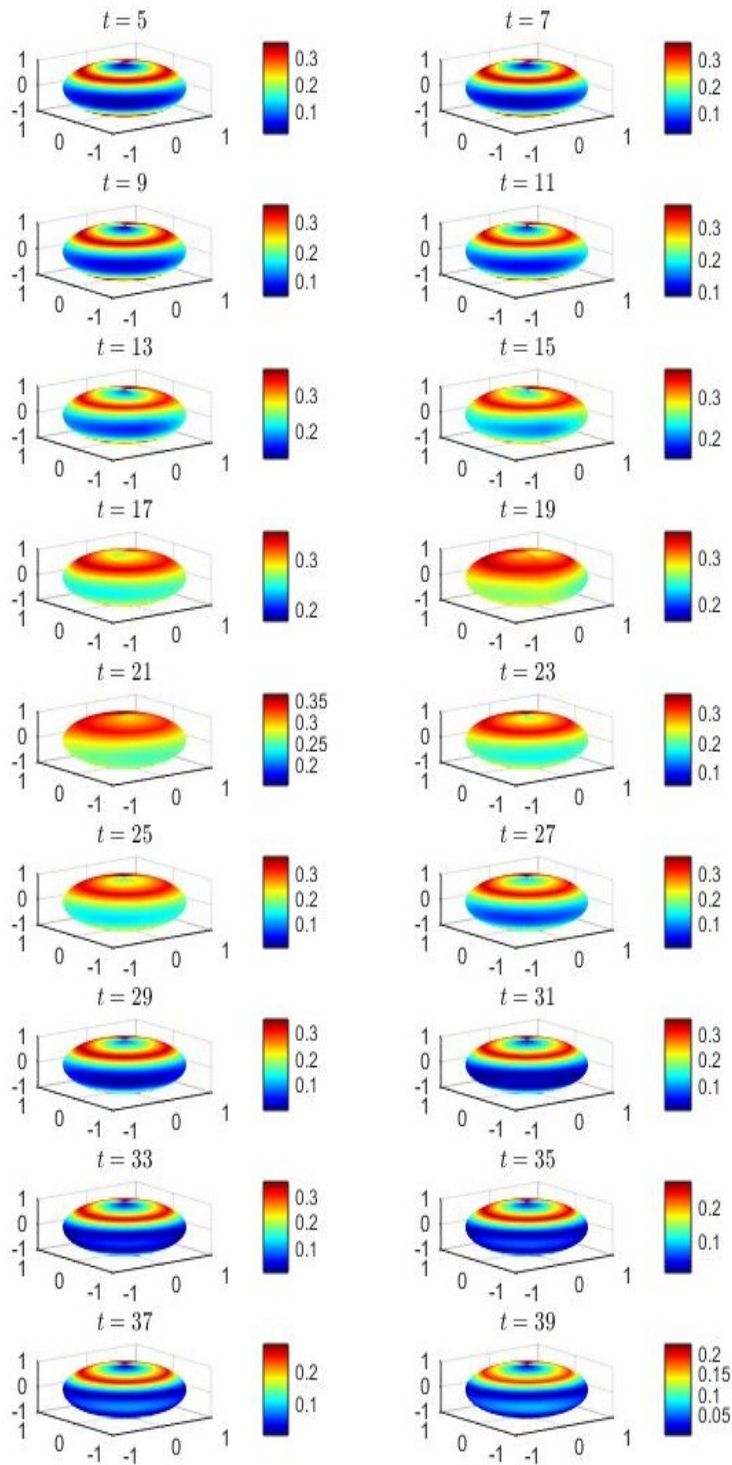


Figure 16: Spherical functional 5-fold-cross validation absolute errors associated with response plug-in regression predictor. Their spherical functional values are displayed at times  $t = 5, 7, 9, 11, 13, 15, 17, 19, 21, 23, 25, 27, 29, 31, 33, 35, 37, 39$



## 6 Conclusions

This paper opens a new research line within the context of multiple functional nonlinear regression from manifold functional data strong-correlated in time. Particularly, the framework of connected and compact two-point homogeneous spaces is adopted. The formulated multiple functional regression model, with functional response, functional regression parameters and time-dependent scalar covariates, goes beyond the assumptions of weak-dependent, and the Euclidean setting usually adopted in the current literature in functional regression. The simulation study and real-data application illustrate the interest of the presented approach, allowing the incorporation of time in the covariates, to represent the evolution of nonlinear associations between the manifold response and regressors. In particular, this aspect is crucial when changes over time arise modifying in a substantial way the manifold patterns of functional response and regressors. On the other hand, the linear case addressed in the Supplementary Material (extended one way FANOVA model to the spatiotemporal spherical context) in a different orthogonal basis framework, allows the prediction of local behaviors in a neighborhood of the pole of the zonal functions considered, which can be of interest in detecting small local changes in the functional response mean in those small areas near the pole.

## Acknowledgements

This work has been supported in part by projects MCIN/ AEI/PID2022-142900NB-I00, and CEX2020-001105-M MCIN/ AEI/10.13039/501100011033.

## References

- [1] Alegría A, Bissiri PG, Cleanthous G, Porcu E, White P (2021) Multivariate isotropic random fields on spheres: Nonparametric Bayesian modeling and  $L^p$  fast approximations. *Electronic Journal of Statistics* 15(1):2360–2392. <https://doi.org/10.1214/21-EJS1842>
- [2] Álvarez-Liévana J, Ruiz-Medina MD (2017) The effect of the spatial domain in FANOVA models with ARH(1) error term. *Statistics and Its Interface* 10(4):607–628. <https://dx.doi.org/10.4310/SII.2017.v10.n4.a7>
- [3] Álvarez-Liévana J, Ruiz-Medina MD (2019) Prediction of air pollutants  $PM_{10}$  by ARBX(1) processes. *Stochastic Environmental Research and Risk Assessment* (33):1721–1736. <https://doi.org/10.1007/s00477-019-01712-z>
- [4] Andrews GE, Askey R, Roy R (1999) *Special Functions*. In *Encyclopedia of Mathematics and its Applications*. Vol 71: Cambridge University Press, Cambridge

- [5] Bosq D (2000) *Linear Processes in Function Spaces*. Springer, New York
- [6] Caponera A (2021) SPHARMA approximations for stationary functional time series in the sphere. *Stat Infer Stoch Proc* (24):609–634. <https://doi.org/10.1007/s11203-021-09244-6>
- [7] Caponera A, Marinucci D (2021) Asymptotics for spherical functional autoregressions. *Ann Stat* 49(1):346–369. <https://doi.org/10.1214/20-AOS1959>
- [8] Cardot H, Mas A, Sarda P (2007) CLT in functional linear regression models. *Probab Theory Relat Fields* 138:325–361. <https://doi.org/10.1007/s00440-006-0025-2>
- [9] Cartan E (1927) Sur certaines formes Riemanniennes remarquables des géométries á groupe fondamental simple. *Ann Sci Éc Norm Supér* 44(3):345–467. <https://doi.org/10.24033/asens.781>
- [10] Crambes C, Mas A (2013) Asymptotics of prediction in functional linear regression with functional outputs. *Bernoulli* 19(5B):2627–2651. <https://doi.org/10.3150/12-BEJ469>
- [11] Cuevas A, Febrero M, Fraiman R (2002) Linear functional regression: The case of a fixed design and functional response. *Canadian J Statistics* 30(2):285–300. <https://doi.org/10.2307/3315952>
- [12] Febrero-Bande M, Galeano P, González-Manteiga W (2017) Functional principal component regression and functional partial least-squares regression: an overview and a comparative study. *International Statistical Review* 85(1):61-83. <https://www.jstor.org/stable/44840871>
- [13] Forster P, Ramaswamy V, Artaxo P, Berntsen T, Betts R, Fahey DW, Haywood J, Lean J, Lowe DC, Myhre G (2007) Changes in atmospheric constituents and in radiative forcing. In: *Climate Change 2007: The Physical Science Basis*. Cambridge University Press, New York, NY, pp 129-234
- [14] Giné E (1975) The addition formula for the eigenfunctions of the Laplacian. *Advances in Mathematics* 18(1):102–107. [https://doi.org/10.1016/0001-8708\(75\)90003-1](https://doi.org/10.1016/0001-8708(75)90003-1)
- [15] Li D, Robinson PM, Shang HL (2019) Long-range dependent curve time series. *J of the American Statistical Association* 115:957–971. <https://doi.org/10.1080/01621459.2019.1604362>
- [16] Ma C, Malyarenko A (2020) Time varying isotropic vector random fields on compact two-point homogeneous spaces. *J Theor Probab* 33:319–339. <https://doi.org/10.1007/s10959-018-0872-7>

- [17] Mas A (1999) Normalité asymptotique de l'estimateur empirique de l'opérateur d'autocorrélation d'un processus ARH(1). *C R Acad Sci Paris* 329(10):899–902. [https://doi.org/10.1016/S0764-4442\(00\)87496-0](https://doi.org/10.1016/S0764-4442(00)87496-0)
- [18] Ovalle–Muñoz DP, Ruiz–Medina MD (2024) LRD spectral analysis of multifractional functional time series on manifolds. *TEST*. <https://doi.org/10.1007/s11749-023-00913-7>.
- [19] Panaretos VM, Tavakoli S (2013a) Fourier analysis of stationary time series in function space. *Ann Statist* 41(2):568–603. <https://doi.org/10.1214/13-AOS1086>
- [20] Ruiz–Medina MD (2011) Spatial autoregressive and moving average Hilbertian processes. *Journal of Multivariate Analysis* 102:292–305. <https://doi.org/10.1016/j.jmva.2010.09.005>
- [21] Ruiz–Medina MD (2012a) New challenges in spatial and spatiotemporal functional statistics for high–dimensional data. *Spatial Statistics* 1:82–91. <https://doi.org/10.1016/j.spasta.2012.02.006>
- [22] Ruiz–Medina MD (2012b) Spatial functional prediction from spatial autoregressive Hilbertian processes. *Environmetrics* 23(1):119–128. <https://doi.org/10.1002/env.1143>
- [23] Ruiz–Medina MD (2016) Functional analysis of variance for Hilbert-valued multivariate fixed effect models. *Statistics* 50:689–715. <https://doi.org/10.1080/02331888.2015.1094069>
- [24] Ruiz–Medina MD (2022) Spectral analysis of long range dependence functional time series. *Fractional Calculus and Applied Analysis* 25:1426–1458. <https://doi.org/10.1007/s13540-022-00053-z>
- [25] Ruiz–Medina MD, Miranda D, Espejo RM (2019) Dynamical multiple regression in function spaces, under kernel regressors, with ARH(1) errors. *TEST* 28:943–968. <https://doi.org/10.1007/s11749-018-0614-2>
- [26] Wild M (2009) Global dimming and brightening: A review. *Journal of Geophysical Research: Atmospheres* 114. <https://doi.org/10.1029/2008JD011470>